Fabrication of Superconducting Tunnel Junction via Double Angle Evaporation

by

Ashish Rana

A Thesis Presented in Partial Fulfillment
of the Requirements for the Degree
Master of Science

Approved May 2019 by the
Graduate Supervisory Committee:

Robert Y Wang, Chair
Nathan Newman
Liping Wang

ARIZONA STATE UNIVERSITY

August 2019

ABSTRACT

This thesis explores the possibility of fabricating superconducting tunnel junctions (STJ) using double angle evaporation using an E-beam system. The traditional method of making STJs use a shadow mask to deposit two films requires the breaking of the vacuum of the main chamber. This technique has given bad results and proven to be a tedious process. To improve on this technique, the E-beam system was modified by adding a load lock and transfer line to perform the multi-angle deposition and in situ oxidation in the load lock without breaking the vacuum of the main chamber. Bilayer photolithography process was used to prepare a pattern for double angle deposition for the STJ. The overlap length could be easily controlled by varying the deposition angles. The low temperature resistivity measurement and scanning electron microscope (SEM) characterization showed that the deposited films were good. However, I-V measurement for tunnel junction did not give expected results for the quality of the fabricated STJs. The main objective of modifying the E-beam system for multiple angle deposition was achieved. It can be used for any application that requires angular deposition. The motivation for the project was to set up a system that can fabricate a device that can be used as a phonon spectrometer for phononic crystals. Future work will include improving the quality of the STJ and fabricating an STJs on both sides of a silicon substrate using a 4-angle deposition.

ACKNOWLEDGMENTS

In the last one and half years, I have had the good fortune of working with so many amazing people at ASU who helped me greatly in completing this thesis. First and foremost, I would like to thank my advisor, Dr Robert Wang for giving me an opportunity to work under his guidance. He has provided me with so many insights on how to approach a research project. He emphasized the importance of reading while doing research. He has also been a great teacher by pointing me to an appropriate source to find an answer to a question.

I would also like to thank all my committee members Dr Nathan Newman and Dr Liping Wang for agreeing to serve on my committee and their kind help and constructive suggestions on my research and manuscript. Prof. Newman who was also a constant help throughout the project. He shared his experience of working with the E-beam system that helped improve the deposition.

Next, I'd like to thank my collaborator Zhongyong Wang, who has helped me with virtually everything on this project, from lithography to reviewing the manuscript. This project couldn't have been completed without his contribution. I also thank all my all other group members Wilson, Prathamesh, Yanan, Matt for all their help in the past one year. I'd also like to thank Tim Karcher from Eyring Materials Center, Richard Hanley, Justin and Bryan from Newman's group, Jim and John from the machine shop, Carrie for help with lithography. They all have been very kind and eager to help.

Lastly, I would like to thank my parents for encouraging me to pursue engineering and being the greatest support both emotionally and financially.

TABLE OF CONTENTS

LIST OF TABLES

Table Page

LIST OF FIGURES

Figure Page

Figure Page

CHAPTER 1.

Introduction and Background

1.1 Motivation

The main motivation for pursuing this project to prepare an E-beam system that can perform multiple angle deposition to fabricate a phonon spectrometer by fabricating Superconducting tunnel junctions (STJ). A phonon spectrometer can be used to measure energy gaps in phononic crystals and nanocrystal superlattices. In a phonon spectrometer, a monochromatic phonon emitted by a phonon emitter on one side of the phononic crystal or nanocrystal superlattice and detected by phonon detector on other side of the crystal if it does not fall in the energy gap range. Apart from this, STJs can also be used as cryogenic sensors for a number of purposes. They can be used as photon detectors by creation of free charge carriers. They are extremely sensitive and can generate the excitation three orders of magnitude more than the classical semiconductors.[1] The traditional method of fabricating a tunnel junction using a shadow mask and oxidizing in atmosphere is not very efficient and is a long process. The double angle deposition method and in-situ oxidation is much faster and produce better tunnel junctions because there is minimum involvement from the user and the chances of human error are less.

1.2 Superconductivity

1.2.1 Background and History

Superconductivity was first discovered by Heike Kamerlingh Onnes in 1911 while cooling mercury.[2] For a normal conductor, as we decrease the temperature, the resistivity decreases and levels off as the temperature approaches 0 K. But in some materials, as the

temperature decreases below a certain temperature called critical temperature the resistivity abruptly drops to zero. This can be seen in Figure 1.

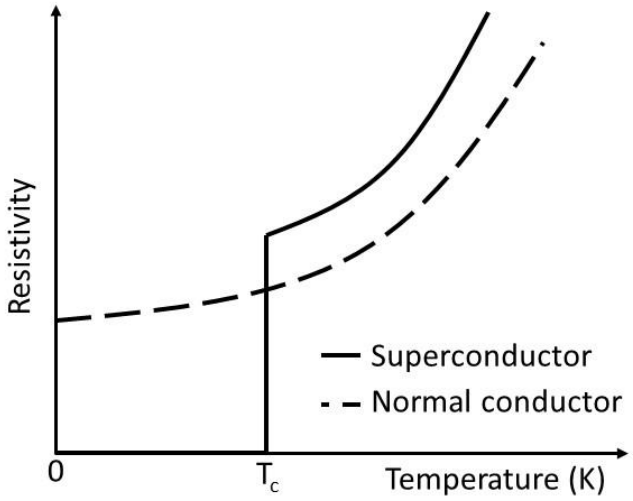

Figure 1: Resistivity of conductors with temperature

When Hans Meissner and Robert Ochsenfeld studied the magnetic behaviour of the superconductors, they found that when the superconductors are cooled in presence of a magnetic field below their critical temperature, the magnetic field was expelled from the interior of the superconductor[3] as can be seen from Figure 2.

It is well established experimentally that the magnetic field will not penetrate the superconductor when under superconducting phase i.e when the temperature is below T_c but as the temperature exceeds T_c, the magnetic field penetrates the superconductor. This is called the Meissner effect. Also, vice versa is true. When then the external applied magnetic field is applied to a superconductor and it exceeds a certain critical value, it breaks the superconducting property of the material. This proves that the magnetic field is another parameter that can control the superconductivity. In addition to magnetic field and

temperature, current density through a conductor exceeds a critical value, superconductivity is lost.

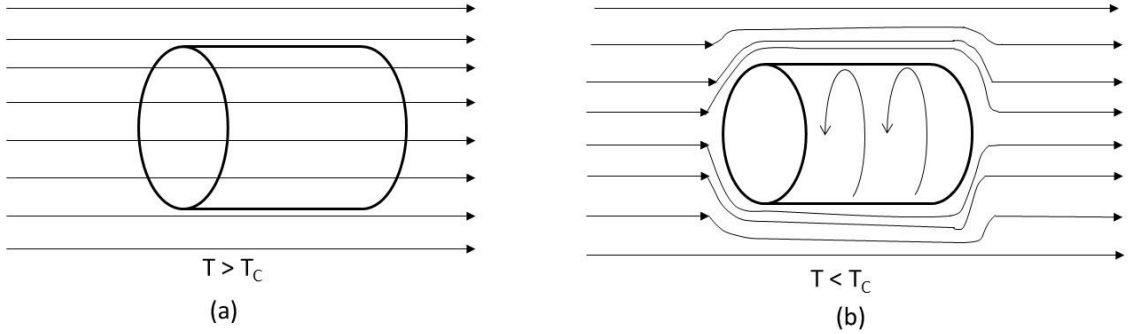

Figure 2: (a) Magnetic field penetrates superconductor when T > Tc (b) Magnetic field is repelled below T < Tc

1.2.2 BCS theory of superconductivity

In 1957, three scientists Bardeen, Cooper, and Schriefer came up with a theory based on quantum mechanics to explain superconductivity in some materials. According to BCS theory, superconductivity arises because of the attraction between the two electrons forming cooper pairs. [4,5] Cooper pairs are formed at extremely low temperature, i.e temperatures below the critical temperature.[6] At low temperatures, the lattice vibration is low, and movement of an electron deforms the lattice that causes a local increase of positive charge in the vicinity of the moving electron. This positive charge attracts another electron toward it. This seems as if the two electrons are attracted to each other. This virtual attraction of the electrons forms a Cooper pair that move together throughout the conductor.

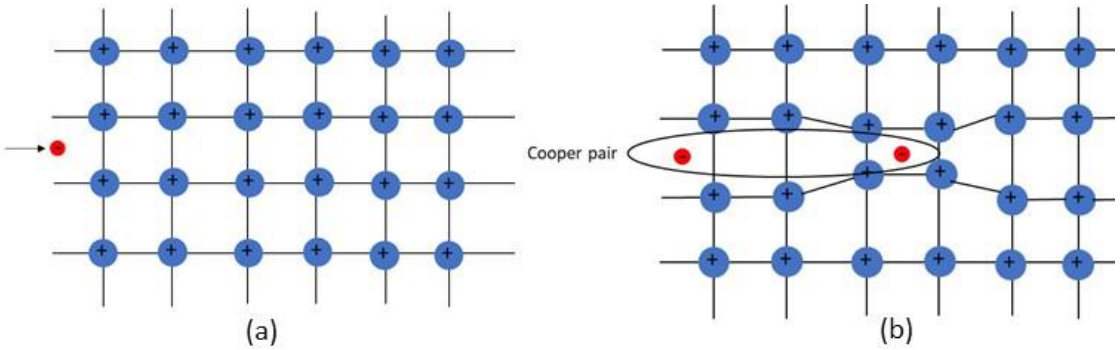

Figure 3: a. An electron moving through the undistorted lattice. b. Distorted lattice causes pairing of electrons to form Cooper pairs

There are many cooper pairs in the conductor that move through it without any resistance from the lattice vibration because it is negligible at temperatures below critical temperatures.

At 0 K, all the electrons are bound together as Cooper pairs. This pairing causes lowering of energy of electrons below the Fermi level that is reduced by binding energy Δ. All the electrons that act as bosonic pairs can be described by a single wave function. At temperatures above absolute zero, some electrons will exist as fermions above the ground state. The binding energy of cooper pairs is a function of the critical temperature of the material as: [7,8]

$$2\Delta(0) = 3.52\ k_B\ T_C \qquad (1)$$

Where Δ is the binding energy of the cooper pairs. Table 1 shows the superconducting gaps and critical temperatures of some of the superconducting metals.

Table 1: Superconducting gaps of some metals[8]

Material	T_c (K)	$2\Delta(0)$ (meV)
Al	1.175	0.34
Nb	9.25	3.05
Pb	7.196	2.73
Sn	3.722	1.15

The free electrons above the Fermi level are called quasiparticle. At temperatures below T_c and above 0 K, the quasiparticle density of states for $|E| \geq \Delta$ is

$$N_s(E) = \frac{2N_0E}{\sqrt{E^2 - \Delta^2}} \tag{2}$$

Where N_0=single spin density at fermi level and N_0=1.72 x 10^{10} $\mu m^{-3}eV^{-1}$ [9]

Using the above equation with the Fermi level distribution equation give the number of quasiparticles as

$$n_{qp} = \int_0^\infty \frac{N_s(E)}{1 + exp\left(\frac{E}{k_BT}\right)} dE \approx 2N_0\sqrt{2\pi k_BT\Delta}\, exp\left(-\frac{\Delta}{k_BT}\right) \tag{3}$$

For aluminum using Δ=1.76 k_B T_C =1.76 k_B (1.2 K) =2.91 x 10^{-23} J= 0.182 meV. Using this quasiparticle density vs temperature is shown in Figure 4. The number of quasiparticle density increases linearly on the log-linear plot so exponentially directly with temperatures.

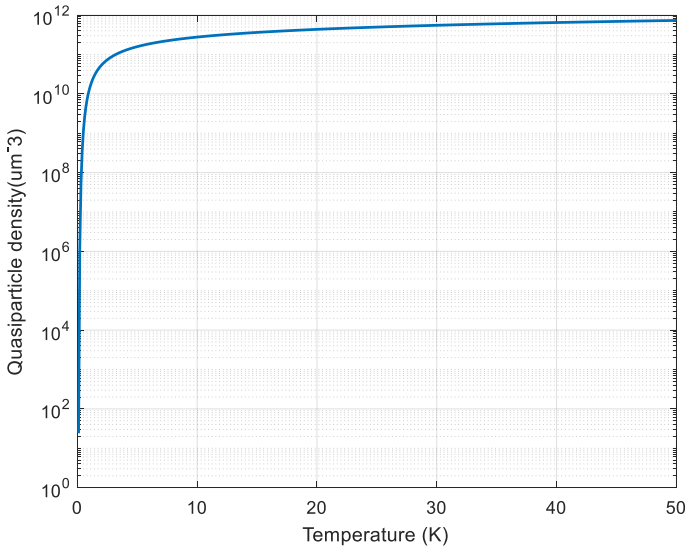

Figure 4: Quasiparticle density above the fermi level

1.3 Superconducting Tunnel Junction

A superconducting tunnel junction (STJ) is a device in which an insulating thin layer is sandwiched between two superconductors. Current through an STJ passes through the insulating layer by electron quantum tunnelling across it. Figure 5 shows an Al STJ on a silicon substrate. Figure 6 shows the energy vs density of states (DOS) diagram of an STJ.

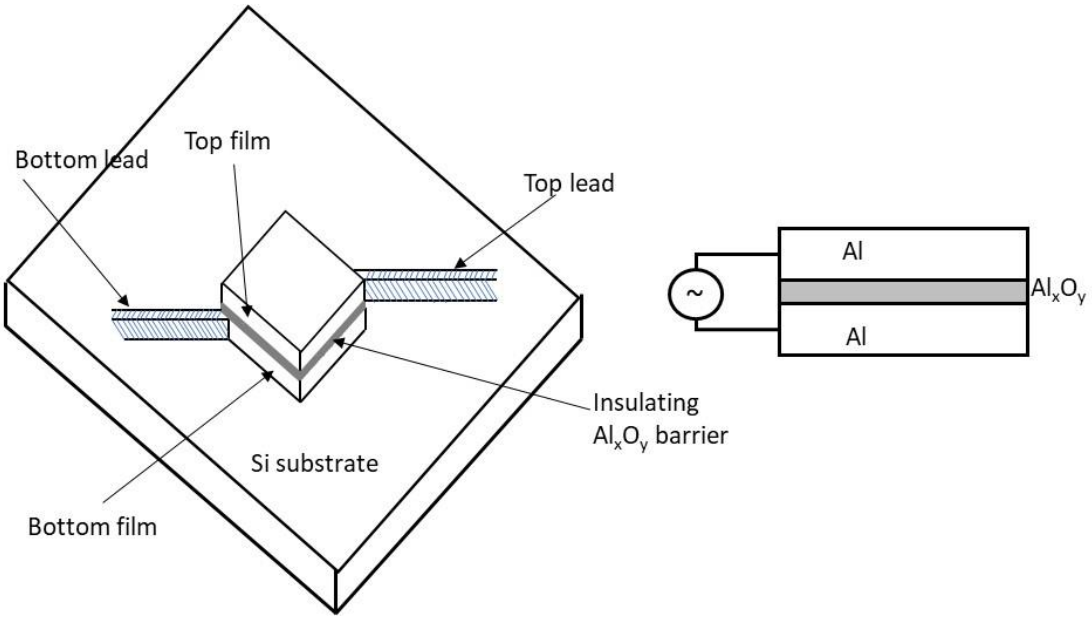

Figure 5: Al Superconducting tunnel junction

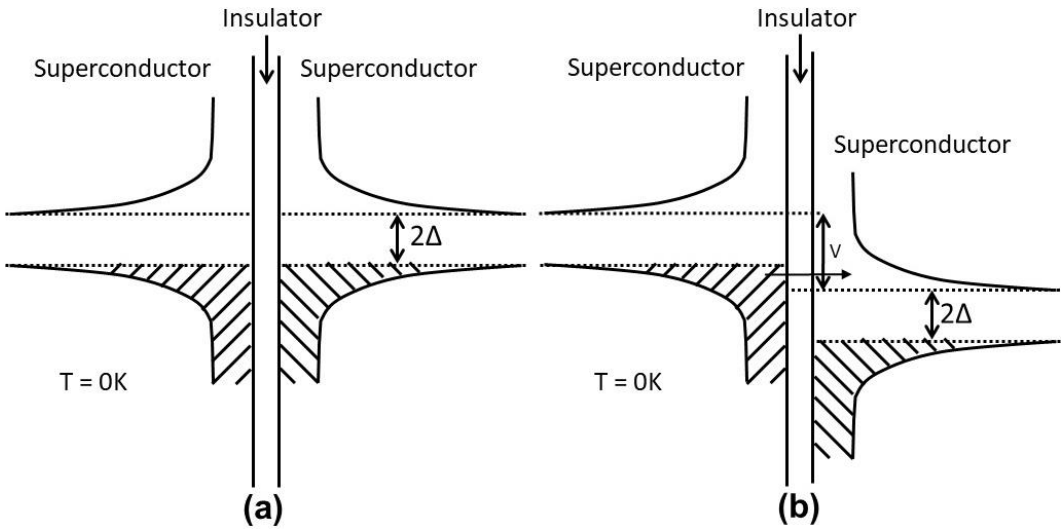

Figure 6: E vs density of states at (a)V=0, (b) V >0

In Figure 6(a), both the superconducting layer on either side of the insulating layer and at absolute zero most of the electrons pair up as cooper pairs and occupy energy below Fermi level. When the voltage is applied across the junction, there is a bias across the two layers that can break the cooper pairs into free electrons that can tunnel across the insulating

layer. But, the current is zero as is evident from Figure 7(a) if the applied voltage is V< 2 Δ/e. Once the voltage exceeds this value, there is a sudden increase in current and after that, there is a linear I-V relation that is predicted by ohms law. It is assumed that the supercurrent is suppressed by external magnetic field in these graphs.

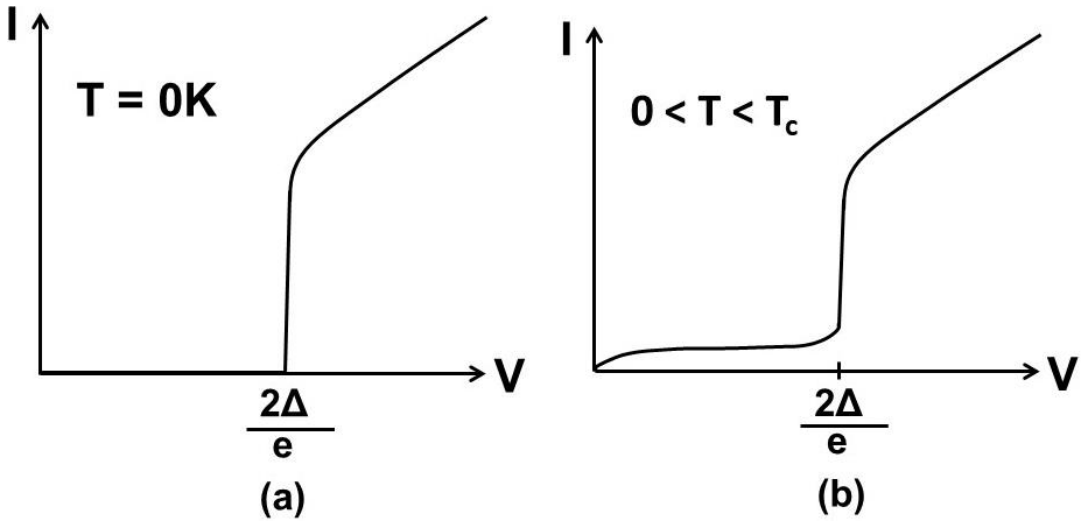

Figure 7: I-V characteristic curve for a superconducting tunnel junction, at T= 0 K and (b) T > 0 K

But we know that it is impossible to reach absolute zero and therefore, Figure 7a is not realistic. Figure 7(b) shows the I-V curve for an STJ for temperature between $0<T<T_C$. Even when the applied voltage is V< 2 Δ/e, there is a non-zero current that can be attributed to already existing free electrons above fermi level that that can tunnel through the insulating barrier.

CHAPTER 2

Results using E-beam System

2.1 Background and assembly of the E-beam system

2.1.1 Revitalizing the old E-beam system

The first task for this project was to make the old E-beam system that was not operated for more than a decade functional. Figure 8 shows the schematic of the E-beam system that was not operational for more than a decade.

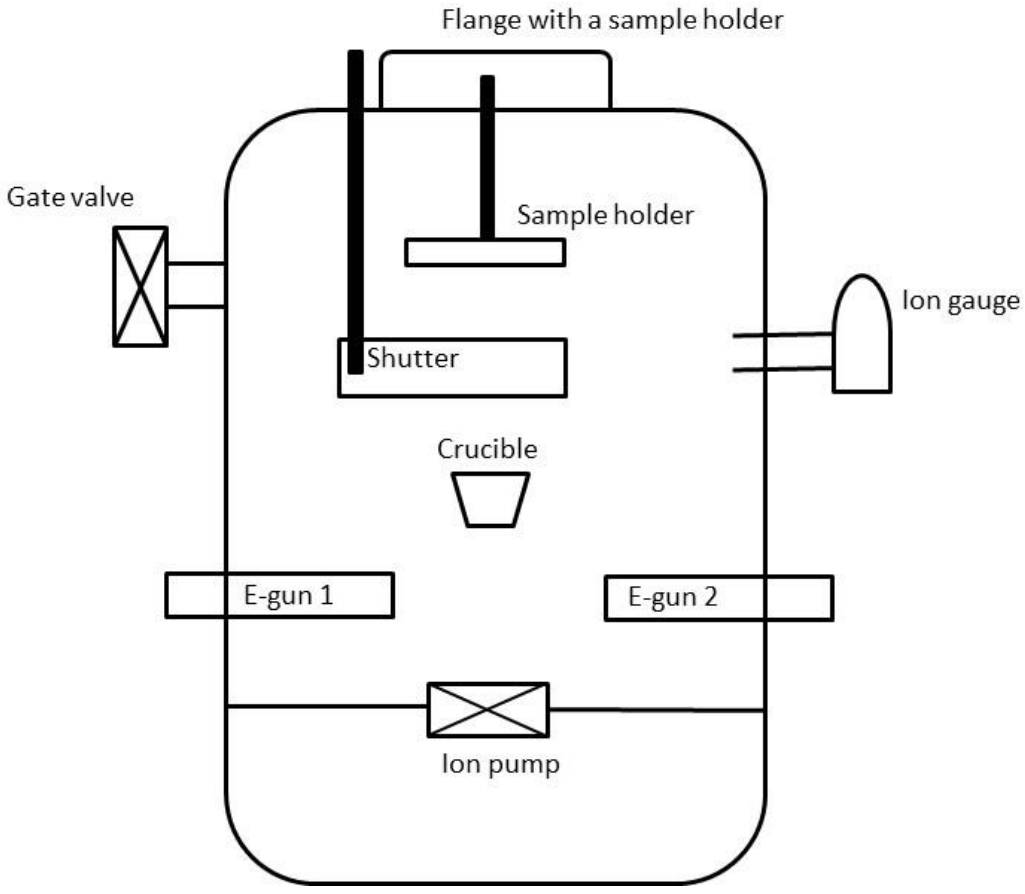

Figure 8: Initial E-beam system with main components

To be able to get it to work for depositing films, the following modifications were made the system:

1. Vacuum pumps: To be able to use the E-beam system for depositing any kind of film, it needs to be pumped to a low pressure using various pumps. The low pressure is imperative to E-beam deposition as it improves the quality of deposition because low number of impurities reduced the probability of contaminants reacting with the sample as well as the reaction with the filament that destroys it. Apart from the contaminants, the gas molecules also reduce the mean free path of the vapour. The following pumps were added to the system to reach a certain level of vacuum.

a. Mechanical pumps: [10,11] It is an essential part of the vacuum system to reduce the pressure to a level so that the turbopump can be started. It is also known as the "Roughing Pump" as it is used in the rough(low) vacuum range. It is sometimes referred to as "Backing Pump" as it is commonly used at the outlet of the turbopump. The mechanical pump shown in Figure 9 was used for getting the pressure down to about 200 mTorr. It is a Rotary vane mechanical pump which is shown in Figure 9.

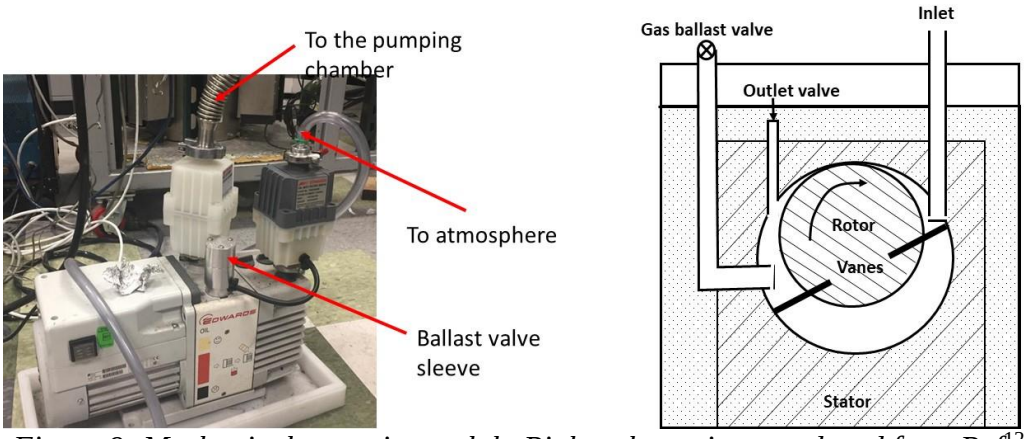

Figure 9: Mechanical pump in our lab. Right schematic reproduced from Ref[12]

b. Turbopumps: To further lower the pressure inside a chamber, turbopumps are used. Figure 10(b) shows a principle operation of the turbopump. A turbopump has a stack of rotors, each having multiple angled blades, rotating at very high speeds between a stack of stators. As a gas particle hits the rotating blades, it gains an additional velocity component from the moving blades thereby speeding it up and pushing it out. The overlaying of these speeds yields a total speed and a direction in which the particle will move. This process of turbo pumping can be used to pump the chamber to as low as 1×10^{-06} Torr using the turbo available in our lab.

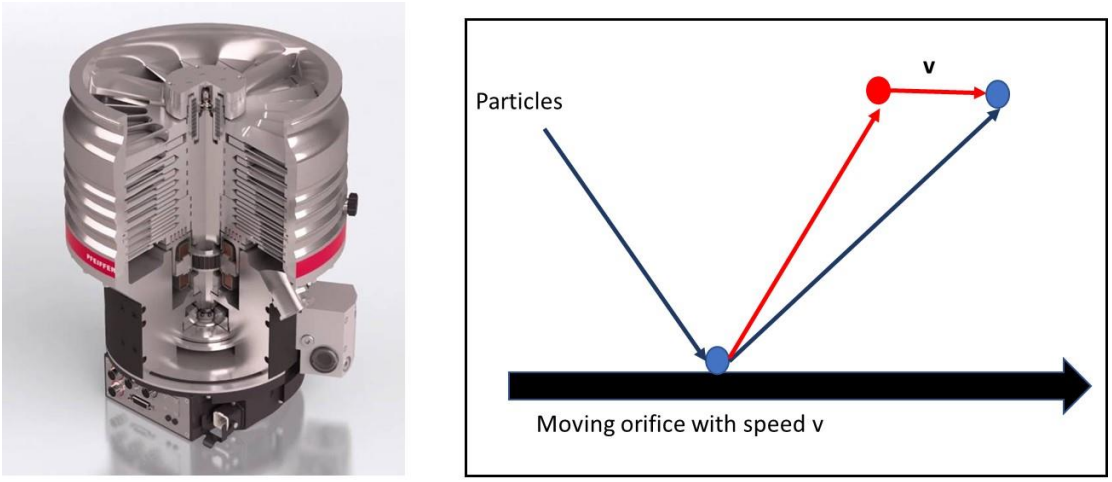

Figure 10: (a) Cross section of turbopump,[13] *(b) Principle behind turbopump*

c. Ion pumps: Although the ion pumps were already part of the system, they needed to be tested for after the low enough pressure was reached using the mechanical and the turbopump. An ion pump is designed to further lower the pressure to as low as 1×10^{-12} Torr. The pump consists of 2 titanium plates acting as cathodes and an array of a parallel stainless-steel tubes acting as anode and a magnetic field parallel to the anode tubes. As the electric field is applied across the two electrodes, the free electrons in the gas atom are

attracted by the positively charged anode. Due to the magnetic field, the electrons move in the spiral direction inside the tubes. This motion increases the probability of the electrons to collide with the gas (O_2, N_2) molecules. The fast-moving electrons form a negative gas ion that is repelled by the anode and is accelerated towards the cathode. As the positively charged ion hits the cathode, it sputters Titanium on anode walls created various titanium compounds like TiO_2, TiO, TiN, TiN_2 etc. Therefore, the pressure reduction is achieved by forming various oxides and nitrides of the gas molecules and hence reducing their contribution to pressure. Over time the cathode plates replaced as there is the limited amount of Titanium for the forming the nitrides and oxides. Ion pumps do not require any roughing pump and must be operated at pressures lower than 10^{-4} Torr.[14, 15] The ultimate pressure that we can reach using our ion pump is $1x10^{-7}$ Torr.

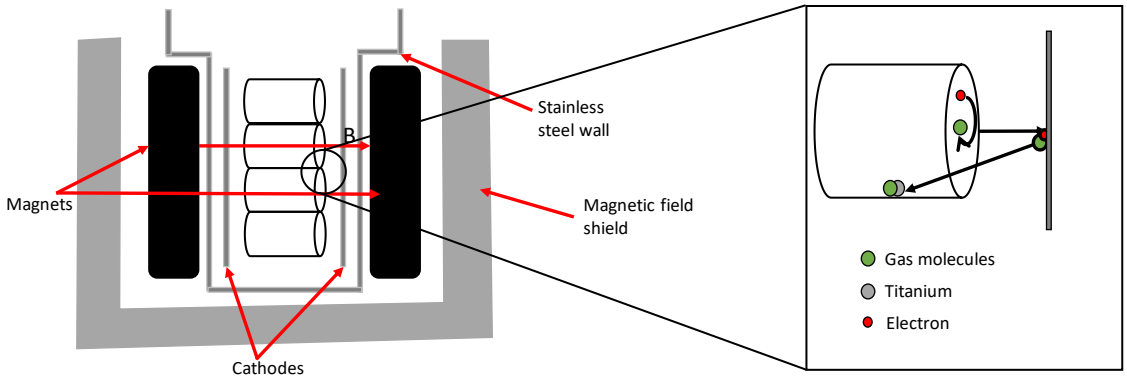

Figure 11: Schematic of the working principle of an ion pump.

2. E-beam system leak:

When I first started working on the project, the vacuum chamber had a leak that prevented pumping it down to low pressures. There are several ways to check to detect a leak in the system depending on the amount of leak rate. [16] The leak was detected by using the following methods in that order:

a. Pressure rise test: This works on the principle that a leak in a chamber will allow a small amount of gas to enter a sufficiently evacuated chamber. In this test, an easily volatile liquid like ethanol or IPA is sprayed on the suspected flanges and we wait for the pressure inside to rise. A leak will result in an increase in the pressure inside the chamber.[17]

b. Foam spray test: bubble test is also useful for detecting high leak rates. In this test, the chamber is pressurized with inert gases like N_2. Then snoop solution is sprayed on the suspected openings and is observed for bubbles. Bubbles are observed at the leak sites.

c. Helium leak check: In this test, He is introduced to the suspected part that is connected to the detector as shown in Figure 12. He is chosen because He molecules are very small and can sneak through even very small leak. The helium travels to the helium detector connected to the test part and the detector shows the increase in pressure.[18]

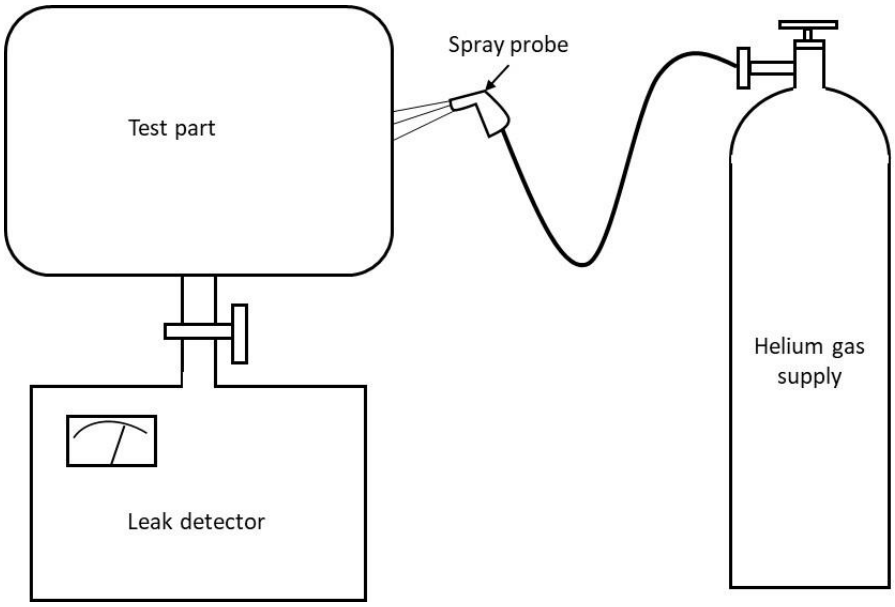

Figure 12: Helium leak detection process.

3. Adding a Crystal monitor: To deposit a film of a particular thickness, crystal monitor is essential. The working of a quartz crystal is based on the piezoelectric effect. The crystal vibrates with its natural frequency when an RF voltage is applied to it. The natural frequency is governed by equation (4).

$$\omega = \sqrt{\frac{k}{m}} \tag{4}$$

As the film deposits the mass increase and the natural frequency changes.[19] This change in frequency can be converted to the thickness deposited. It is important to maintain a constant temperature of the crystal to avoid change in the natural frequency, so the cooling water is continuously run through the crystal holder.

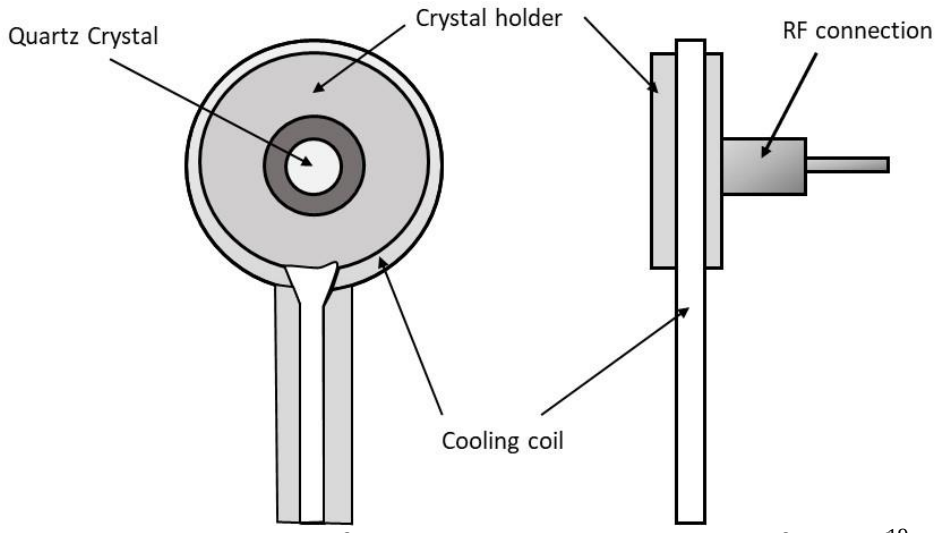

Figure 13: Schematic of the crystal monitor. Reproduced from Ref[19]

4. Adding cooling water connections: When the electron guns are operated during the deposition process, a thousand of volts applied to them that heats up the guns. To cool the electron guns and the crucible that contains the evaporating material, cooling water connections are made to prevent them from overheating.

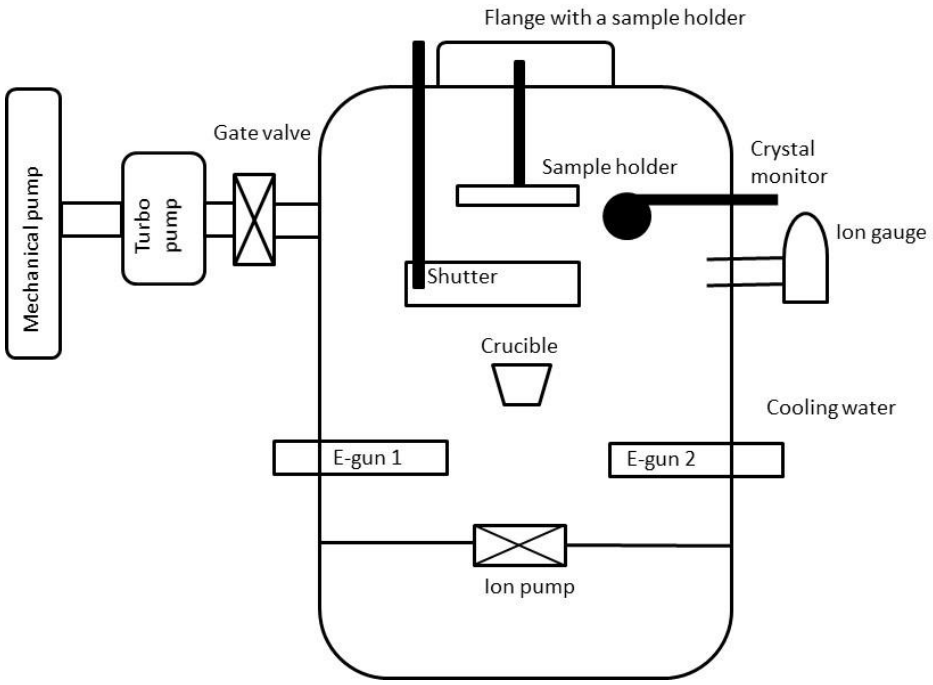

Figure 14: Modified E-beam system with main components

Figure 14 shows the modified E-beam system that is now ready to deposit a plain film. The section covers the deposition and characterization of a plain film deposited using the E-beam system shown in Figure 14.

2.2 Single thin film deposition using E-beam system

When depositing a film using E-beam system, certain steps need to be followed in a particular order. Figure 15 illustrates the physical vapour vacuum deposition in an E-beam system. Since deposition involves applying high voltages to electron guns, be sure to make sure the all the components on the system are grounded. To avoid the crucible and e-guns from overheating, let the cooling water run for 5-10 minutes before the deposition. When the high voltage is turned ON, high energy electron is accelerated by the magnetic field pointing into the plane. The electron beam hits the aluminum in the crucible and melts it. Since the vapour pressure of the aluminum vapour is of the order of 10^{-5} Torr inside the

vacuum chamber, it evaporates at the temperatures much lower than its boiling temperature at atmospheric pressure. It evaporated equally in all directions and is deposited on the substrate. A shutter blocks the vapour until a constant evaporation rate is reached.

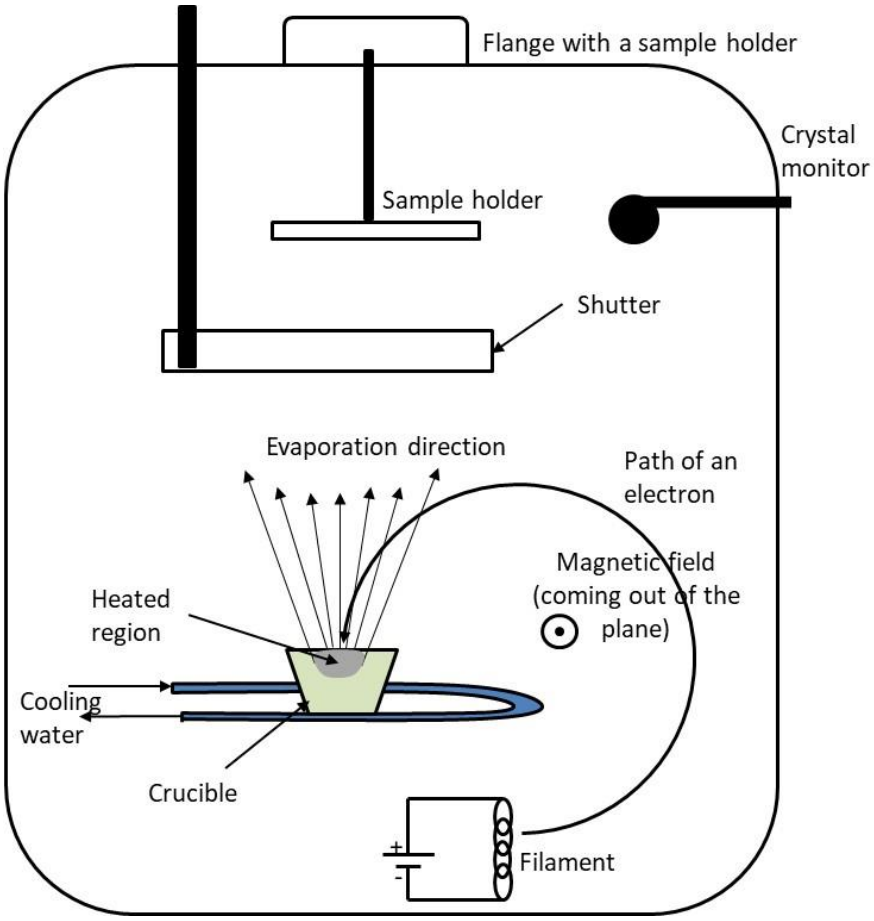

Figure 15: Vapour deposition in the E-beam system

While applying the high voltages to the E-guns to control the deposition rates, one needs to know that the emission current does not vary linearly with the deposition rate. The voltage applied to the E-guns is 4 kV. Figure 16 shows that the deposition rate is exponential. Therefore, one needs to careful while increasing the deposition rate. To get better control, a 10-turn potentiometer should be used.

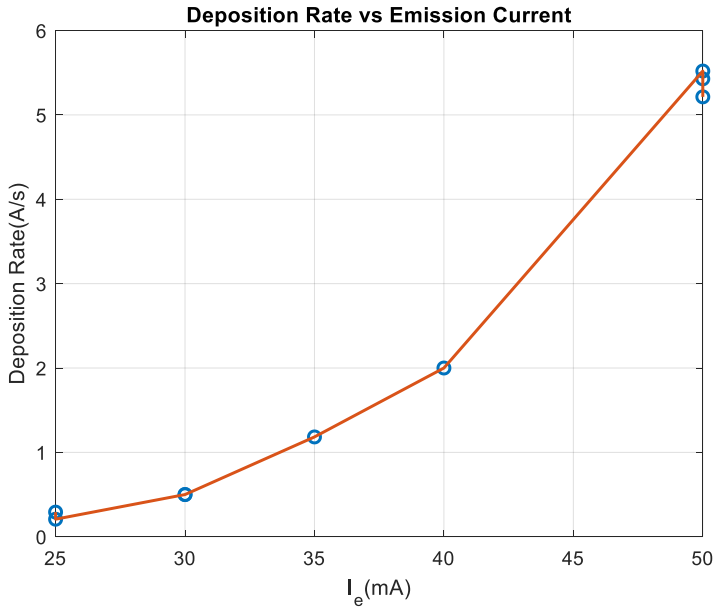

Figure 16: Plot showing deposition rate against emission current

2.2.1 Temperature dependent resistivity of films

Before determining the quality of the tunnel junction, we measured the quality of the plane films deposited using the E-beam system by doing a temperature dependent resistivity analysis.

The resistivity was experimentally measure by using in-line 4-probe method shown in Figure 17. This method measures the sheet resistance by measuring the voltage and current in the configuration shown in the figure and compensates for by multiplying with a correct factor that depends on geometry and dimensions (in this case s and a) of the sample.

Sheet resistance, $R_s = CF\left(\frac{V}{I}\right)$, resistivity, $\rho = R_s t$

Where, CF is correction factor and t, is the thickness of the sample

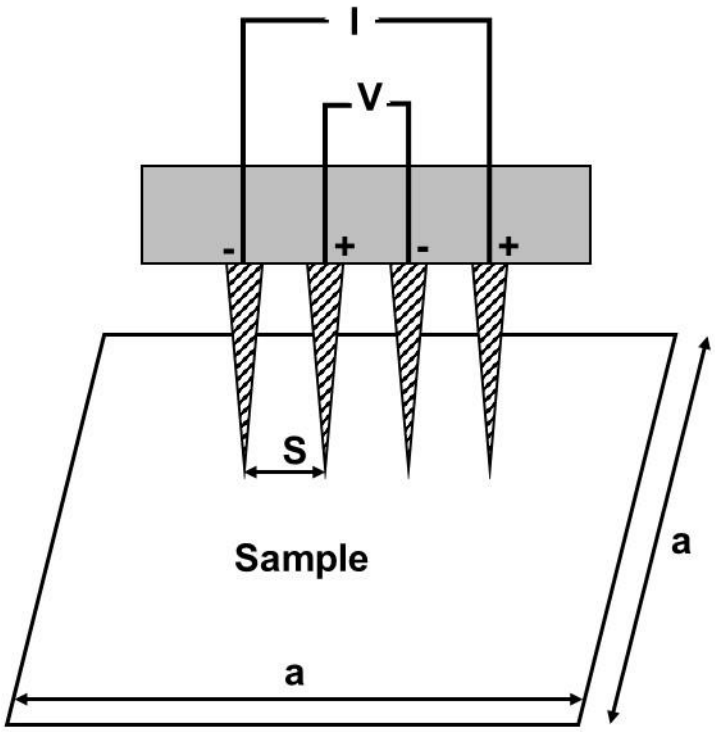

Figure 17: Schematic of in-line 4-point probe method

According to Matthiessen's rule, the relaxation time is given by

$$\frac{1}{\tau} = \frac{1}{\tau_L} + \frac{1}{\tau_i} \tag{5}$$

Where τ_L and τ_i are relaxation times for scattering by phonons and impurities respectively.

$$\rho = \rho_l + \rho_r \tag{6}$$

Where ρ_l is the resistivity due to contribution from the thermal motion of the lattice vibration, also known as phonon resistivity; ρ_i is the residual resistivity that originates from the electron-impurity interaction and is independent of temperature.[20,21] At absolute zero, there are no lattice vibrations due to the thermal fluctuations. Therefore at 0 K, ρ_l=0 and it increases with increasing temperature. Figure 18(a) shows a perfect lattice with only phonons and Figure 18(b) shows a lattice with phonons and impurities.

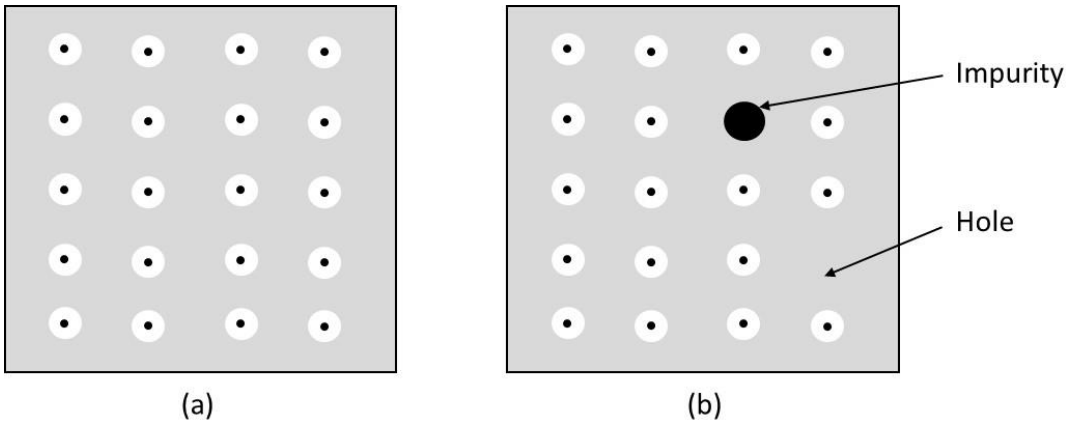

Figure 18: Electrical resistivity is due to electrons collisions with(a)phonons, (b) impurity and holes. Reproduced from Ref[22]

The following expression given by Block-Greisen equation describes resistivity dependence on temperature.

$$\frac{\rho_l}{\rho_{\theta_R}} = \alpha_R \left(\frac{T}{\theta_R}\right)^5 \int_0^{\frac{\theta_R}{T}} \frac{x^5}{(e^x - 1)(1 - e^{-x})} dx \qquad (7)^{21}$$

Where θ_R - Debye temperature and ρ_{θ_R}- resistivity at T=θ_R and α_R is a constant depending on Debye frequency, plasma frequency and electron-phonon coupling

As we the temperature decreases, the contribution from electron-phonon interaction is almost negligible and the electron-impurity interaction dominate the total resistivity. Therefore, it is interesting to define a resistivity ratio based on temperature.

The residual resistivity ratio is defined as the ratio of resistivity at ice bath temperature (i.e. 273.15 K) and resistivity at 4.2 K

$$RRR = \frac{\rho_{T=273{\cdot}15K}}{\rho_{T=4.2K}} \qquad (8)$$

A higher resistivity ratio means that there are lesser contaminants in the material. Metals normally have higher RRR and alloys comparatively lower as theta is a mixture of many metals. Resistivity can be used to calculate the relaxation time of electrons as

$$\tau = \frac{m^*}{ne^2\rho} \tag{9}$$

m^*- electron effective mass (kg)

e - elementary charge on an electron (C)

n – number density of valence electrons (m^{-3})

Taking effective mass equal to the free electron mass, $m^*=m_e$

And n= 18.1 x 10^{28} m^{-3} [23] for Al

Similarly, the mean free path of electrons can be calculated as

$$\Lambda = v_F\tau \tag{10}$$

where v_F=2.03 x 10^6 m/s fermi velocity for Al

The experimentally measured resistivity with temperature is shown in Figure 19. It was measured for films with different thickness. As the temperature decreases, resistivity also decreasing because the electron-phonon scattering is reduced and becomes negligible at for temperatures lower than about 35 K and resistivity. At temperatures lower than this, there is a constant contribution to resistivity from only electron-impurity scattering. Impurities can exist either in form of a foreign particle presence or due to the vacuum that exist because of a missing particle.

When comparing the two 70 nm films deposited at different deposition rate, the resistivity was found to higher when the deposition rate is lower. Krueger and Pollack[24]

describe the initial oxidation of Al thin films at room temperature. They measure the change in mass of 100 nm Al film when the oxygen pressure is 5 x 10^{-7} Torr. This is close to the partial pressure of oxygen during deposition in our chamber. Based on the graph given in this paper, mass fraction of oxygen to aluminum was calculated and is shown in *Table 2*. Since the slower deposited film contains 2.5 times more oxygen, it contributes to impurity scattering that much more and hence shows higher resistivity.

When the 1st (70 nm, 5.4 Å/s) and third film (50 nm, 5.4 Å/s) were compared, the thinner film had higher resistivity which can be attributed to greater grain boundary scattering. De Vries[25] and Hanaoka[26] et al. have shown that resistivity increases with decreasing thickness. The grain diameter is directly proportional to the thickness[25]. This statement is also experimentally supported by our measurement of the grain size using SEM. The grain diameter for 70 nm and 50 nm films were 200 nm and 150 nm respectively. The smaller grain size leads to more grain boundary scattering. The surface scattering contribution can be ignored because the grain size is much bigger than the both thickness and mean free path of the electrons. Therefore, most the electrons will undergo grain boundary scattering before reaching the surface.

Table 2: Oxygen concentration in Aluminum films

Thickness (nm)	Deposition rate (Å/s)	m_{O2}/m_{Al}
70	5.4	1.2 x 10^{-3}
70	1.2	3.3 x 10^{-3}
50	5.4	1.11 x 10^{-3}

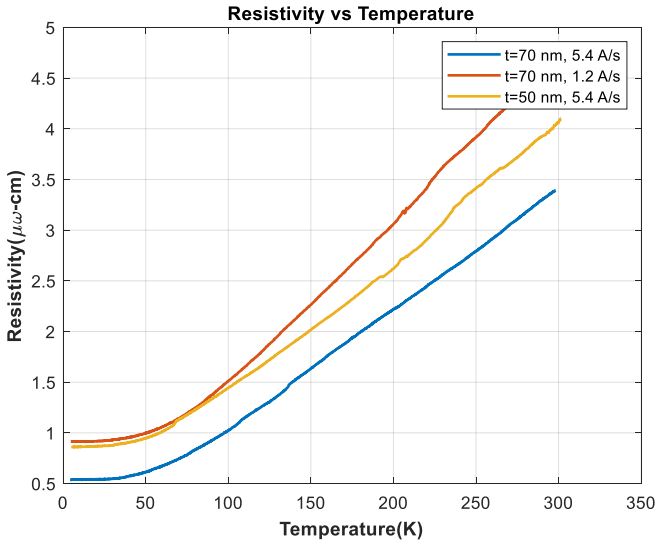

Figure 19: Resistivity vs temperature for aluminum films

When these experimentally measured values were compared with theoretical values obtained using in Figure 20 using Block-Greisen equation, it is observed that the measured values are significantly larger than theoretically calculated values. It reassuring to see that the two graphs are parallel. This hints that the behaviour of resistivity is the same. Only difference between the two is that theoretical calculation does not consider impurity, boundary, surface scattering etc. which is the reason why it approaches zero as the temperature approaches zero. This proves that impurity scattering is not affected by temperature. The numerical values for Block-Gruneisen graph were taken from Meaden.[27]

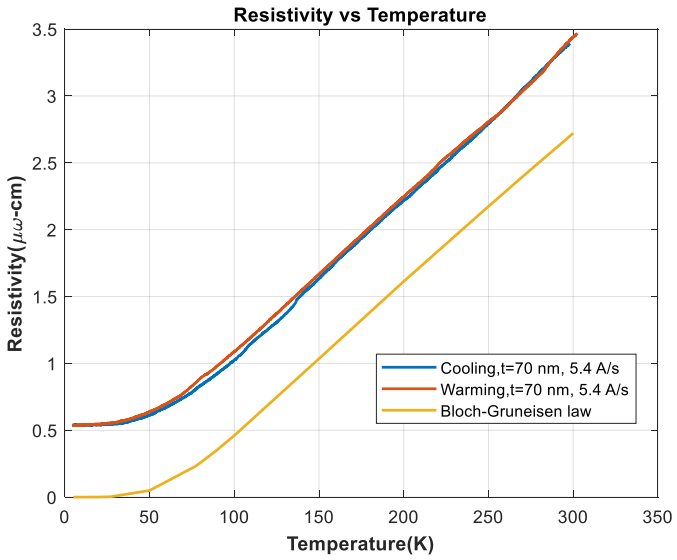

Figure 20: Experimental and theoretical resistivity vs temperature

The mean free path of different films is shown in Figure 21 shows that the mean free path is higher at lower temperature and tends to become constant after the temperature is below 20 K. This is explained by very small lattice vibrations at and the only contribution is from the electron-impurity interaction.

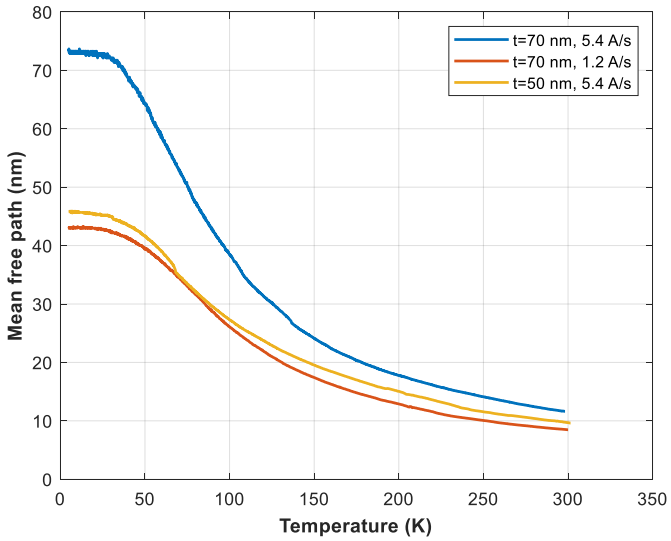

Figure 21: Mean free path vs temperature plot of different Aluminum films

2.2.2 Scanning Electron Microscope (SEM) film characterization

Film characterization was done using Scanning electron microscope (SEM). It can be seen in Figure 22 that both films of the same thickness of about 70 nm when deposited at different deposition rates, the grain size is smaller when deposited at higher deposition rate. Figure 22(a) and Figure 22(b) are deposited at 5.4 Å/s and 1.2 Å/s respectively.

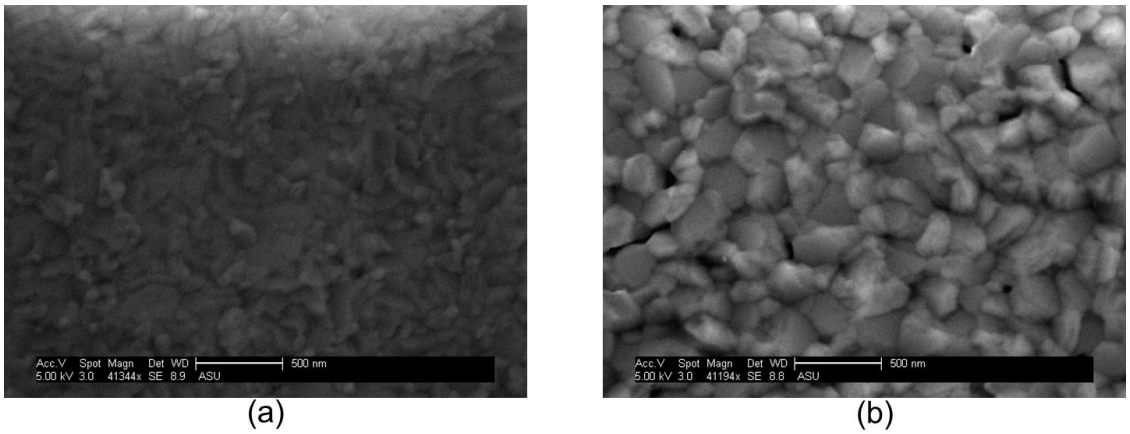

Figure 22: SEM images of the thin film deposition at deposition rate (a)5.4 Å/s, with grain diameter 200 nm (b)1.2 Å/s, with grain diameter 230 nm

2.3 Double Angle deposition

2.3.1 Preparing the E-beam system for Double Angle deposition

The E-beam system setup shown in Figure 14 is still not good enough to carry out the double angle deposition without breaking the vacuum of the main chamber. It was observed in the past that the shadow mask technique that was used in the past required breaking the vacuum and exposing the entire system to the atmosphere. This technique did not yield a good result for the fabrication of the superconducting tunnel junction.

Therefore, an alternative technique of fabrication was designed to get better results. Figure 23 shows the schematic of the double angle evaporation technique that needs to be designed.

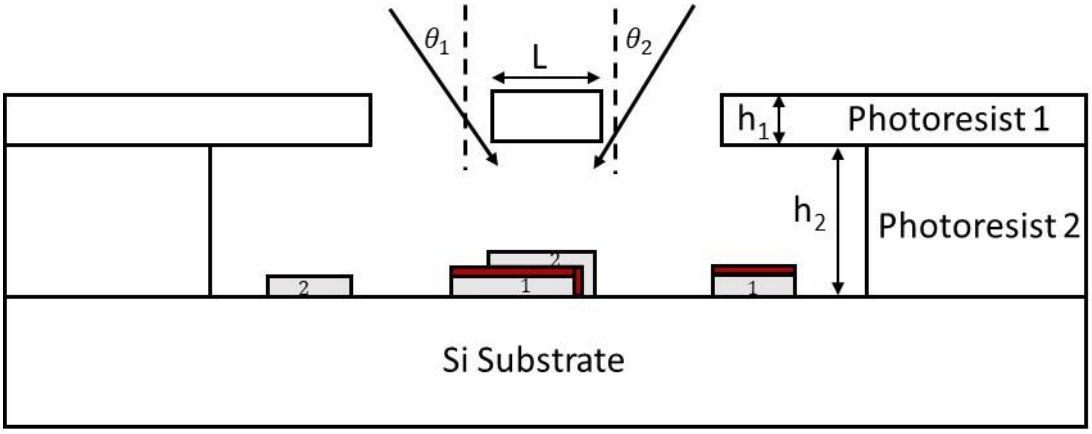

Figure 23: Schematic of double angle evaporation

So, to be able to do the process shown in Figure 23, we need to make further modifications to the E-beam system. Figure 24 shows the schematic of the E-beam system with all the important parts labelled that can be used to perform the double angle deposition. Not only is this process more convenient but also much faster and provides better yield. Figure 25 shows the picture of the main chamber with the all added accessories.

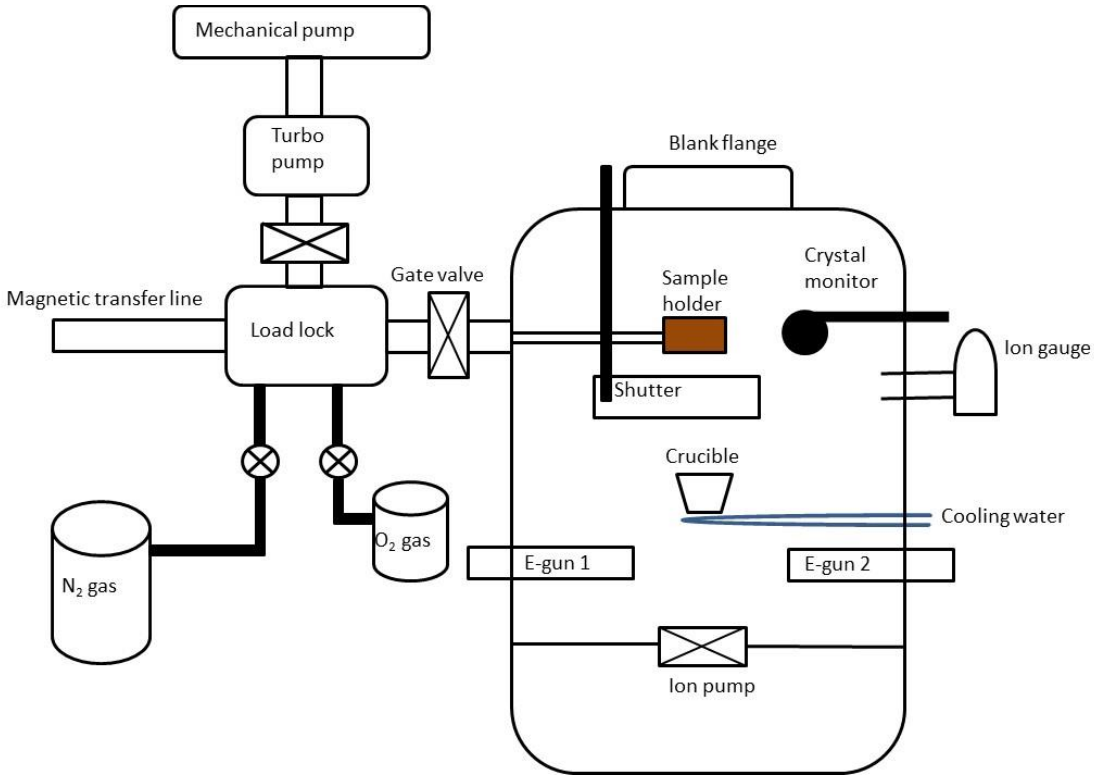

Figure 24: Schematic of the Vacuum system

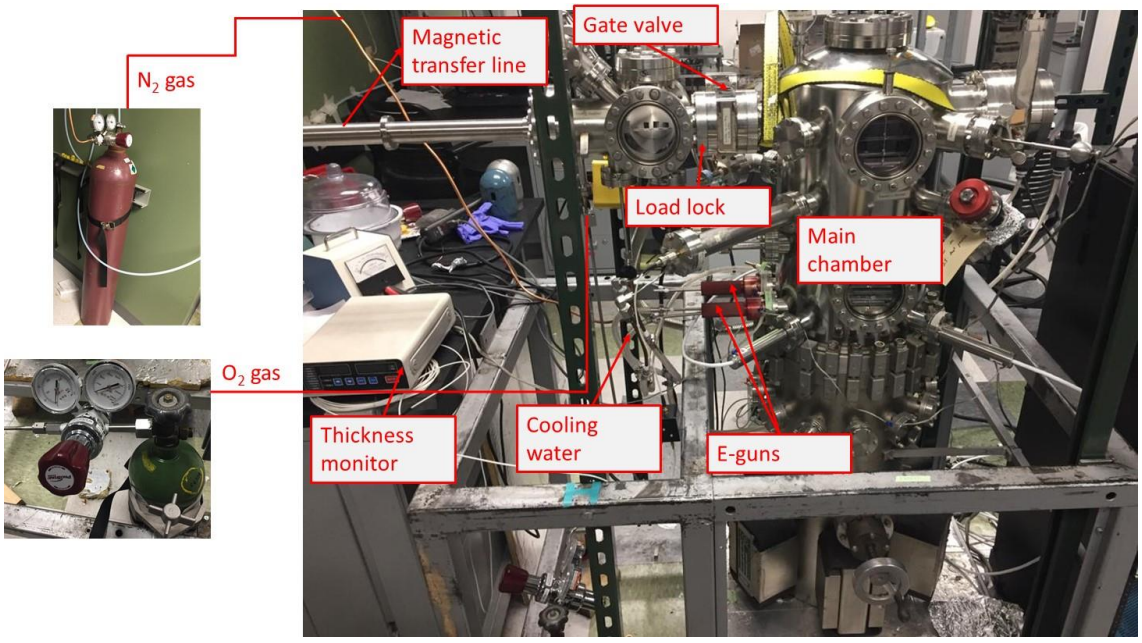

Figure 25: Picture of the main vacuum system

The following parts were added to the system enable the double angle deposition:

1. Load lock: Load lock is an essential part of the system for performing double or multiple angle deposition. Load lock is added to the system to be able to perform multiple depositions without breaking the vacuum every time a new film needs to be deposited. It is also imperative to carry out the oxidation process by isolating the sample in the load lock while the main chamber is still under vacuum. An oxygen line connects the load lock to the O_2 and allows the pure oxygen to be introduced inn to the load lock without breaking the vacuum of the chamber. Pumping the load lock down to a low pressure is significantly after than the main chamber because it is 1/50 times the volume of the main chamber. A venting line also connects it to a N_2 cylinder that is used for venting the chamber instead of introducing atmospheric air that contains reactive O_2 gas.

2. Magnetic transfer line: The magnetic transfer line in Figure 26 is attached to the load lock and used to transfer the sample in and out of the main chamber. Sample holder shown in Figure 27 was fabricated in the machine shop. It is attached to the tip of the shaft of the transfer line to which the samples are mounted. The angular dial is magnetically coupled with the shaft to allow the linear and rotary motion of the shaft. The deposition angle can be adjusted by using an angular scale on the dial.

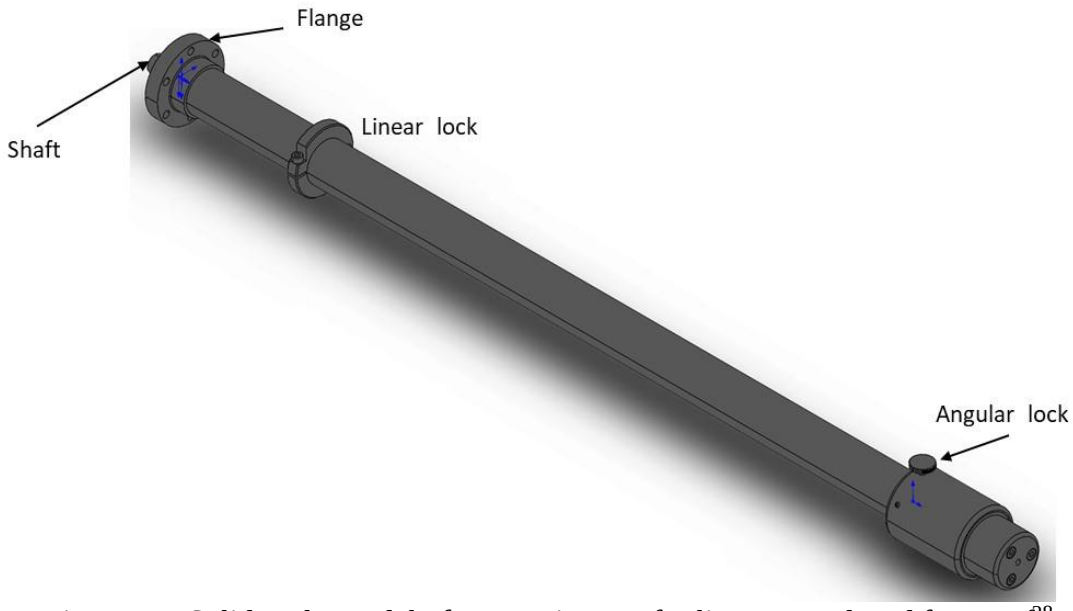

Figure 26: Solidworks model of Magnetic transfer line. Reproduced from Ref[28]

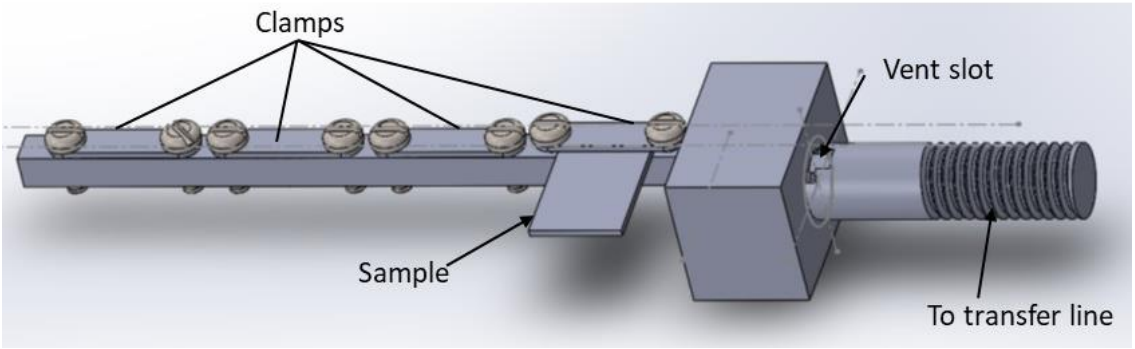

Figure 27: Solid works model of the sample holder

2.3.2 Fabrication of the pattern using Bilayer photolithography

The pattern shown in Figure 23 was prepared using photolithography. Figure 23 that bottom photoresists are much thicker than the top photoresist. The bottom photoresist is essentially a Lift of Resist (LOR) that can be etched away in a developer without exposing it to UV light. The thickness of the two layers depends on the viscosity of the photoresist and the spin speed. Depending on the type desired applications different photoresists can be chosen.

For the bottom photoresist, a lift of resist LOR20B was chosen. For the top photoresist, a positive photoresist AZ3312 was chosen. Figure 28 shows the empirical relation between the spin speed and film thickness of the photoresist for different photoresists.

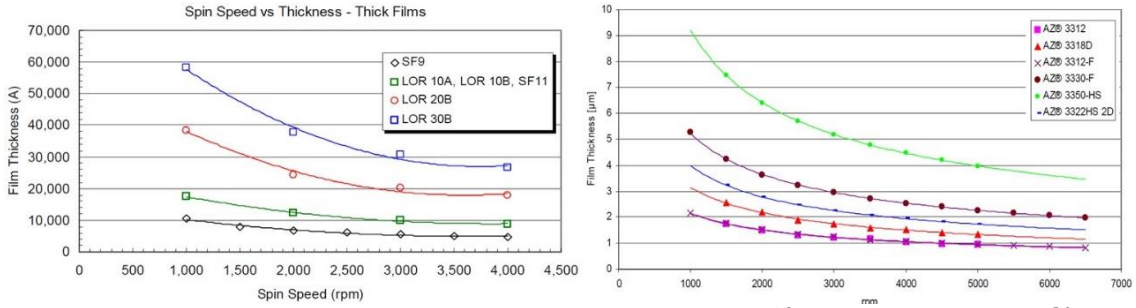

Figure 28: Film thickness vs spin speed, LOR20B (left)[29] *and AZ3312 (right)*[30]

Below is the stepwise procedure for creating the desired feature for deposition:

1. First, the LOR20B is spun on the silicon substrate at 2500 rpm to get about a 2 μm thick layer. Then it is baked at 180 ˚C for 60 seconds to vaporize the solvent and harden the LOR to further improve adhesion to the photoresist.

2. The photosensitive AZ3312 photoresist is spun at 3500 rpm to get a uniform film of about 1 μm. It is then baked at 100 ˚C for 60 seconds.

3. Expose the photoresist to UV light for 6 seconds. The UV light is illuminated by 350 W short arc mercury lamp. Post-exposure bake is performed at 110 ˚C for 60 seconds.

4. For the final step, a developer solution CF26 is used to etch away the exposed photoresist. Developer time will determine the amount undercut. Developer time of about 90 seconds was used.

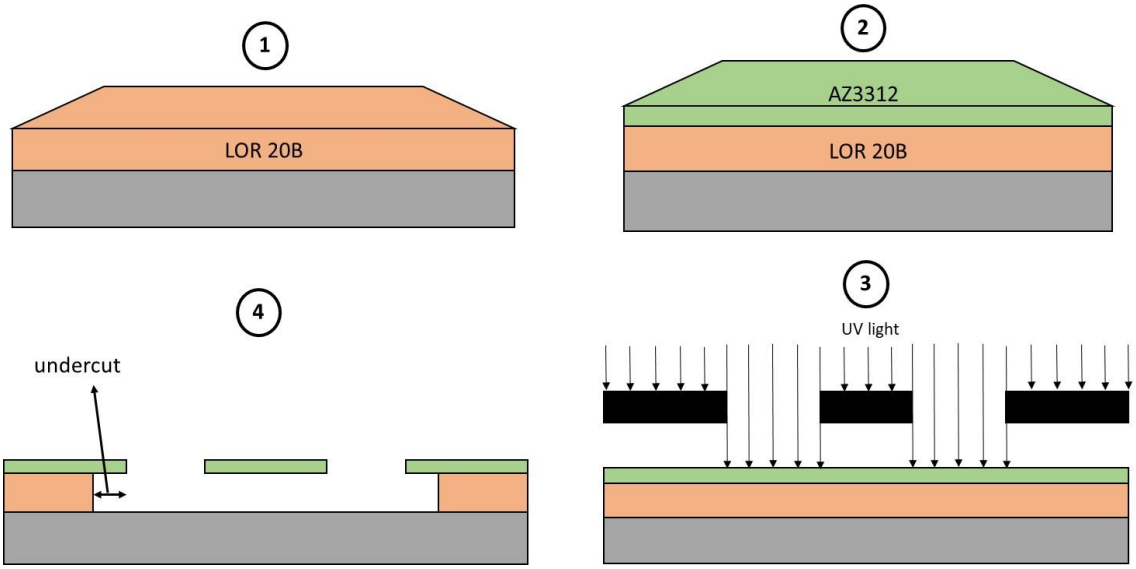

Figure 29: Steps involved in bilayer lithography of the substrate

Figure 30 shows the post-development image of the pattern that can now be used for double angle deposition. Figure 30(b), shows the top view of the pattern shown in Figure 30(a). Region B has only one layer of photoresist, therefore it looks differently than A which has both the layer of photoresist. Length of B is called the undercut. The actual undercut will not be as sharp as shown in this figure.

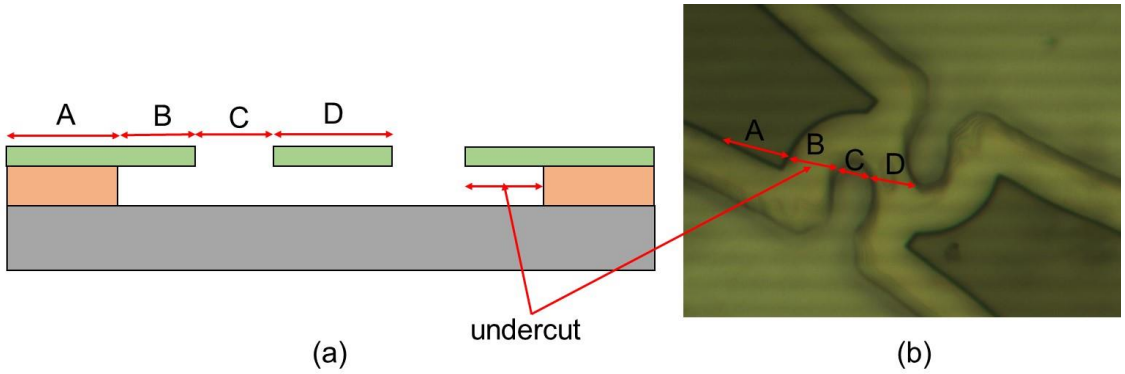

Figure 30: Post development image of the substrate under an optical microscope

2.3.3 Deposition angle calculations

A stepwise procedure for double angle deposition is illustrated in Figure 34. Before the deposition, the angle of deposition needs to be calculated based on the dimensions of the pattern prepared as shown in Figure 31. The thickness can be controlled by either choosing different photoresist or by varying the spin speed for the photoresists. Length L is fixed by the photomask pattern. The following calculations are however performed for dimensions shown in Figure 31.

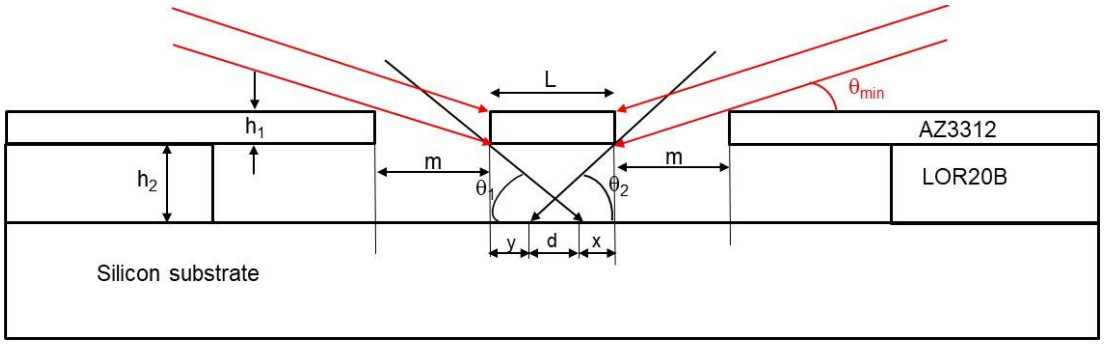

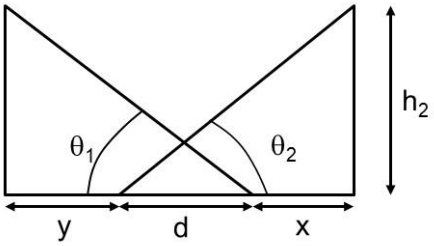

$$Overlap, \mathrm{d} = h_2(\cot\theta_1 + \cot\theta_2) - L$$

$$\theta_{min} = \tan^{-1}\left(\frac{\mathrm{h}_1}{\mathrm{m}}\right)$$

Figure 31: Dimension of the pattern used for deposition.

The deposition angle is very sensitive. It is clear from the graph shown in Figure 32 that to get an overlapping junction, $20^0 < \theta < 34^0$. For our purposes, θ=25^0 was chose to give an overlap of 3 μm (theoretically calculated). Figure 32 shows the graph of junction overlap length vs then deposition angles. Choosing a thicker LOR photoresist offers greater range for these angles. Thicker the photoresist, greater range but the challenge is to make

a uniform layer during spin coating which becomes more difficult as the viscosity of the photoresist increases. Another way to expand the range is to choose a thinner top photoresist.

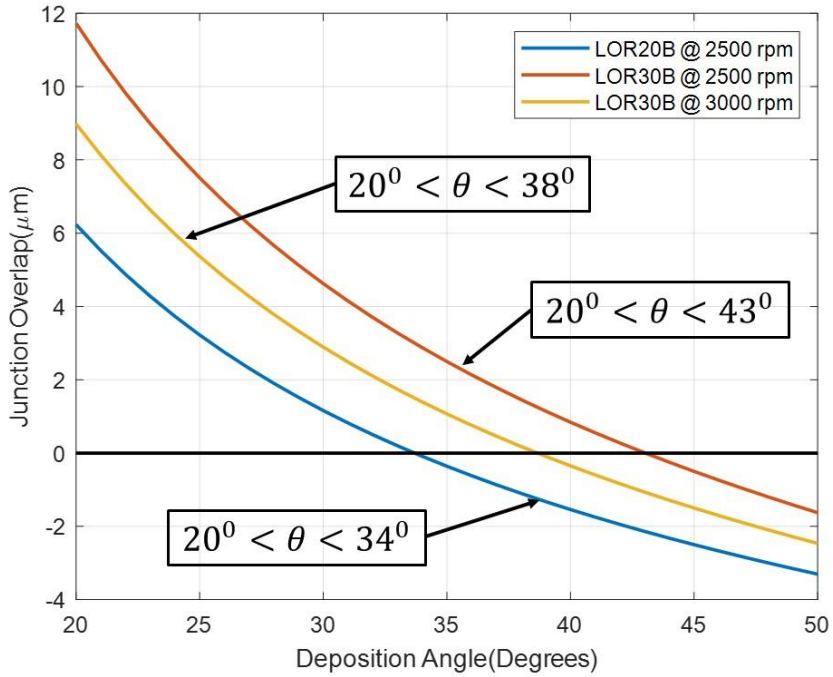

Figure 32: Junction Overlap length vs Deposition angle

2.4 Deposition and in-situ oxidation of the tunnel junction

2.4.1 Deposition

Figure 31 shows the two directions for a deposition. For simplicity, we chose the two the two angles to be equal in both directions i.e. $\theta_1=\theta_2=\theta=25^o$. Before deposition, it is important, to ensure that the all preliminary steps needed to operate the E-gun power supply are followed. The detailed procedure is mentioned in the appendix. The magnetic transfer line is used to orient the sample in the correct position. It is important to adjust for the offset angle (10^o) before the fixing the deposition angle. The offset because the sample is

not perfectly above the crucible. Therefore, an offset is needed to make it normal to the deposition direction. After the first layer of deposition, it is withdrawn into the load lock and 2nd layer is deposited in the other direction. Finally, the lift of process of photoresist is performed by dissolving it in Remover PG. The deposition conditions are listed in Table 3.

2.4.2 In-situ oxidation

The in-situ oxidation along with multi-angle evaporation forms the essence of this thesis. According to electrochemical theory of oxidation after the initial formation of adherent oxide layer that is formed when metal is directly exposed to oxygen, the oxidation reaction is moves forward by movement of ions and electrons through this layer. In most metals the movement of metal ions and equivalent electrons move outward to meet the oxygen ion at the oxide gas interface because the O_2^{2-} is too heavy to diffuse inside. Figure 33 shows the mechanism of oxidation in metals.

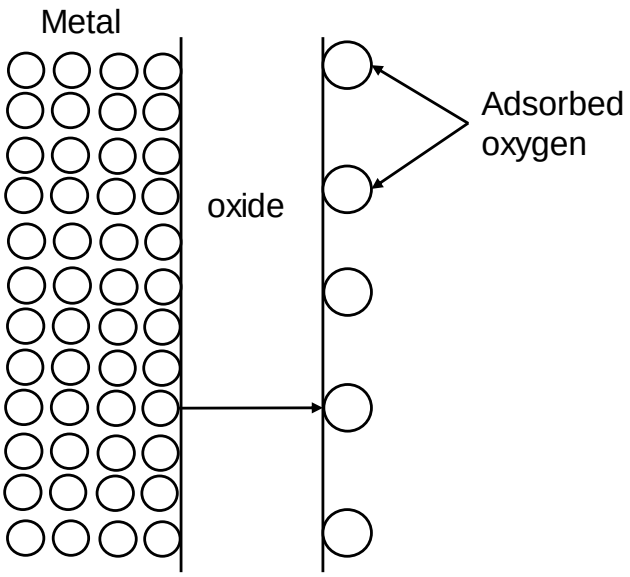

Figure 33: Mechanism showing oxidation process in metals

The process consists of 3 steps:[31] (i) transfer of metal across the metal-oxide interface, (ii) diffusion of metal ions and electrons through the oxide layer, (iii) adsorption of O_2 at oxide-gas interface. The rate of oxidation is initially controlled by (i) and it is independent of the partial pressure of oxygen until a thin layer of oxide is formed. Process (iii) controls the rate if the partial pressure is too low. With the increasing film thickness, process (ii) becomes the rate controlling process and eventually becomes the main rate controlling factor.

Mott[33] proposes that aluminum follows the parabolic law as shown in equation (11). Where x is the thickness, t is the time and constants Ω, D and n are volume of oxide per metal ion, diffusion coefficient of ions and concertation of atoms in oxide respectively.

$$x^2 = 4\Omega Dnt \qquad (11)$$

In the same paper, Mott performed the calculation for the maximum oxide thickness using the above theory for aluminum at room temperature and found that the maximum thickness of the oxide is 4 nm.

The oxidation pressure in our case was maintained at about 0.5 Torr for 30 minutes. From literature search, the estimated oxide thickness in our case is 4-5 nm.

After the oxidation process the 2^{nd} layer is deposited in the same manner as the first layer but at a different angle. Table 3 show the deposition conditions for the tunnel junctions. Figure 34 shows the stepwise procedure for fabrication of the tunnel junction post the preparation of the pattern using lithography.

Table 3: Deposition conditions

Base pressure	1×10^{-7} Torr
Deposition pressure	1×10^{-6} Torr
Deposition rate	5.4 Å/s
Static oxidation	@ 500 mTorr for 30 minutes
Deposition angle	25^{o} (symmetrical on both sides)

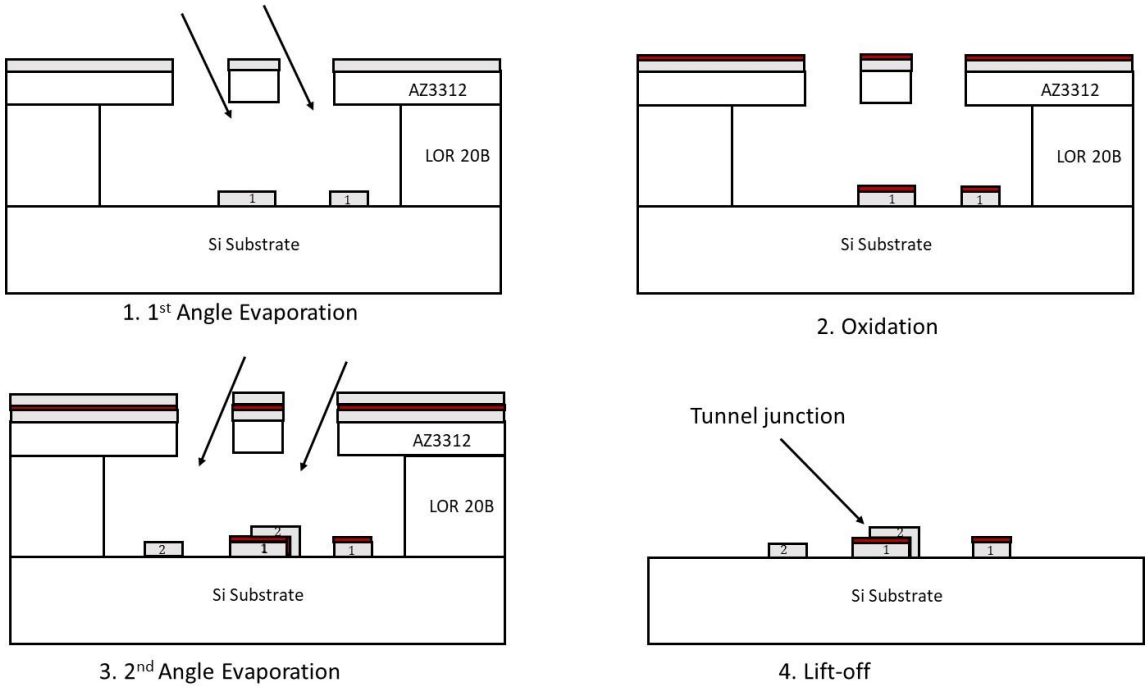

Figure 34: Stepwise schematic of the double angle deposition

One of the successfully deposited tunnel junction is shown in Figure 35. Measurement using SEM (Figure 35b) showed the dimension of a square junction to be 3.2 μm x 3.2 μm. This is very close to the theoretically calculated value of 3 μm for deposition angle 25^{o}. The length of overlap was repeated twice for 25^{o} and the overlapping lengths was 3-3.5 μm in both cases. This goes to show that the double angle deposition method is an effective way of controlling the size of the junction as well is much faster than the traditional methods that use shadow mask.

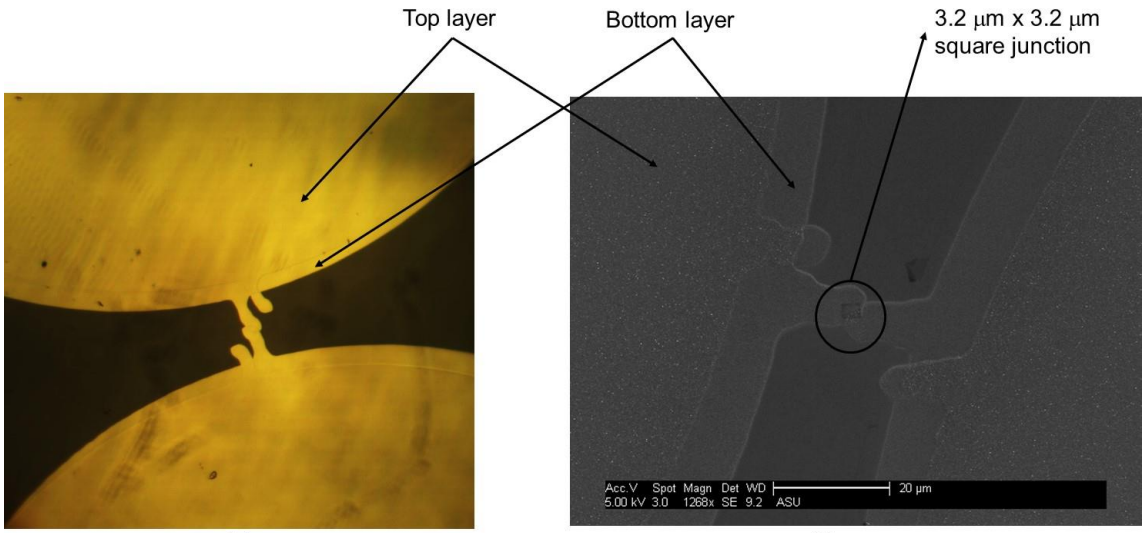

Figure 35: (a) Optical image of the overlapping junctions, (b) SEM image of the overlapping junction

2.5 Storage and wire bonding of the tunnel junction

The fabricated tunnel junctions should be stored in antistatic containers. These bags are used for storing electronic components to prevent damage from electrostatic discharge. They are made up of polyethylene terephthalate (PET) and coated with a layer of plastic. Static free containers dissipates any charge to the ground and thereby prevents the buildup of any static charge on the surface.[34,35]

These bags/containers are also coated with a thin layer of tallow amine on the surface. Tallow amine has affinity for moisture in the room and thereby creates a bridge between the containers and the ground or atmosphere. Therefore, it important to ensure the room has enough humidity to create this path especially during wire bonding of the tunnel junction to the sample holder. This forms an 'antistatic' in the true sense.[36] These

containers/bags are usually pink or red but black bags also exist wherein polyethylene also contain small amounts of carbon.[35]

These bags are effective in preventing the buildup of charge as long as the user is also grounded during the wire bonding of the tunnel junction. So, to prevent the junction from damage, it is important to use static free containers, always maintain proper relative humidity and ground yourself while touching the tunnel junction.

CHAPTER 3.

Testing the Superconducting Tunnel Junction

3.1 Overview of the cryostat

Figure 36 shows the schematic of the Cryostat in our lab. The main parts include an insulated Dewar that is used that holds liquid helium. The Dewar prevents heat transfer to the environment to the atmosphere with a vacuum gap between its inner and outer layers. The space between the two layers is pumped out to create a vacuum and avoid any heat transfer due to convection. Then the most important part for performing the experiment, Inner Vacuum Chamber (IVC) is initially dipped into liquid nitrogen to reduce the temperature from room temperature to 77 K. During this process, He gas is continuously blown through the two sippers to prevent the liquid nitrogen from entering the inside of IVC. Liquid nitrogen can freeze when the temperature is further lowered using liquid He and therefore block the sippers. Then liquid nitrogen is removed and is replaced by liquid helium. Because of the capillary effect, liquid He enters sippers and wraps around the charcoal pump and 1-K pot. It is extremely imperative to maintain a vacuum inside the IVC to prevent the temperature rise. IVC is pumped to about 1×10^{-7} Torr using a turbopump. To suppress the magnetic field produced by the sample, an electromagnet is used to apply a counter magnetic field. The cooling process to base temperature is explained in detail in the following section.

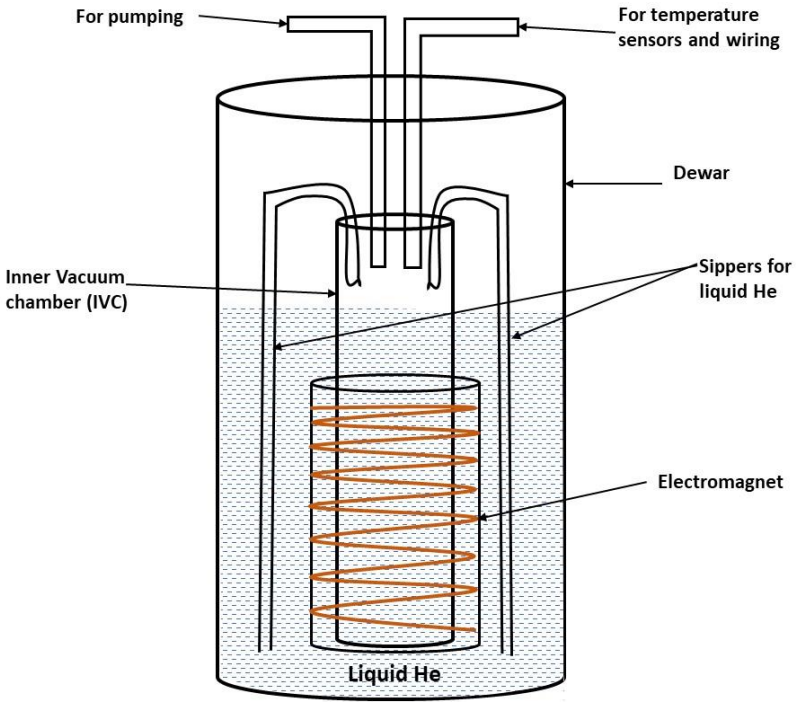

Figure 36: Schematic showing main parts of the Cryostat

3.2 Cooling to base temperature

Figure 37 shows the schematic of cooling the cold head or He-3 pot that then cools the sample holder through conduction. In the schematic Inner vacuum chamber (IVC) is removed to better illustrate the working. The IVC is immersed in the dewar that is then filled with liquid nitrogen to cool it down to 77 K. He gas is blown through the sippers to avoid liquid N_2 from entering the IVC. After the outer IVC is cooled to 77 K. to further cool it down to the base temperature, liquid N_2 is removed and replaced by liquid ^{4}He to reduce the temperatures down to 4.2 K.

To further lower the temperature, charcoal is gradually heated to 45 K to desorb ^{3}He gas absorbed by it. This desorbed gas is continuously cooled and condensed by ^{4}He

that runs through the coil outside the 1-K pot. The heated ^{4}He is continuously pumped out by using a rough pump and the flow rate is adjusted by a needle valve. The condensed ^{3}He liquid drops down and is collected in the cold head. After all the ^{3}He is condensed, the charcoal pump is turned off (stop heating the charcoal). As the charcoal the cools down to attracts the ^{3}He that evaporates from the cold head. In this case, the charcoal acts as a virtual pump. The evaporation of the ^{3}He causes cooling that helps to cold head to reach the base temperatures. The cold head cools the sample holder through conduction. The base temperature of about 0.3 K can be reached using this pressure which is below 1.2 K which is the critical temperature of aluminum.

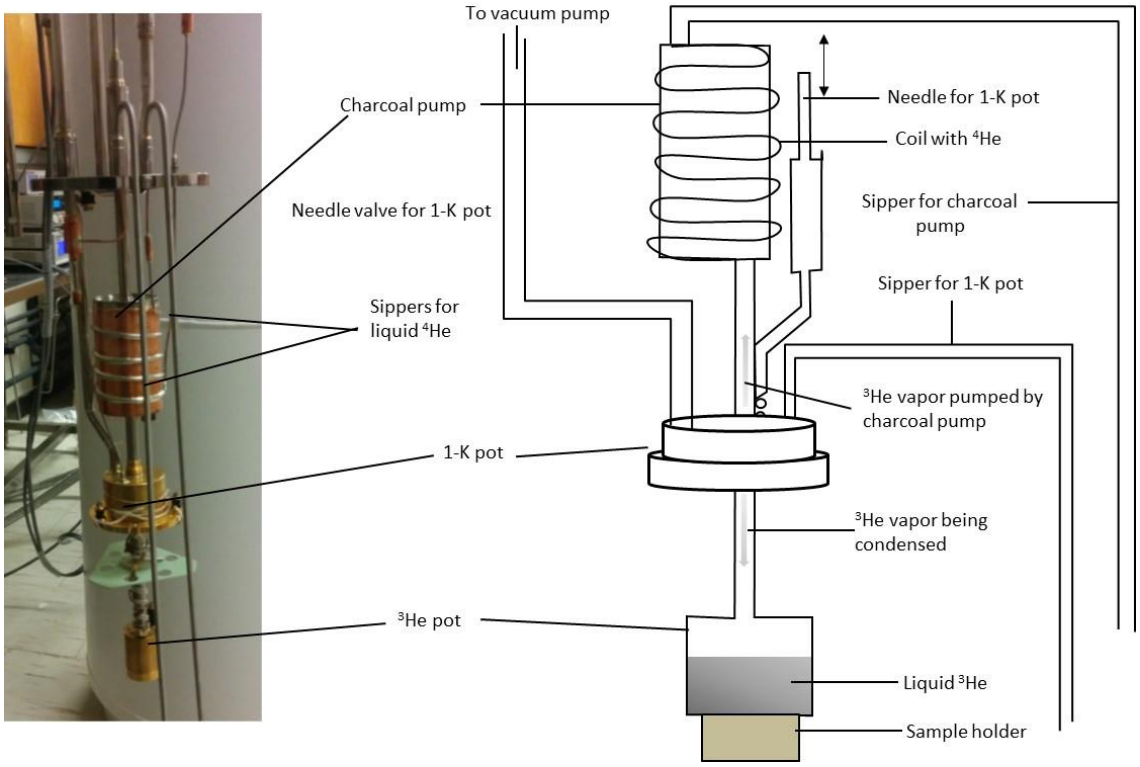

Figure 37: Schematic of the operating principle of He-3 cryostat.

3.3 Tunnel junction quality measurement

3.3.1 Rowell's criteria for a good tunnel junction

To determine the quality of a tunnel junction, John Rowell gave three criterions called Rowell Criteria. [37]

1. The first criteria states that resistance of the barrier varies exponential with its thickness of the insulting barrier.
2. The relation between the differential conductance (dI/dV) and voltage bias is non-Ohmic and parabolic which should be fitted to theoretical model by Brinkman–Dynes–Rowell[38] and Simmons.[39,40] Akerman et al.[41,42] have shown experimentally that the first two criteria are not sufficient in ruling out the presence of pinholes in the insulating barrier.
3. The third and final criterion says that the conductance of the barrier is temperature dependent. Although the first two criterion were proved to be unreliable, this criteria has been very effective in distinguishing the a good junction from the shorted (with pinholes) ones. [40,42]

In addition to the Rowell's criteria, Miller[43] et al. have shown in there paper that in a perfect junction, $I_cR_n \approx 0.8 \times 2\Delta$. I_c is the critical current and R_n is the ohmic resistance after the critical voltage.

3.3.2 I-V Curve measurements

The I-V measurement was performed using a source meter using a 4-point resistance measurement technique. 4-point measurements are more accurate than the 2-point measurement because it does not measure the resistance of the lead wires that would

contribute to the resistance especially if the test resistance is small. The 4-wire measurement schematic is shown in Figure 38. In this technique a current is sourced through a battery and voltage across the sample resistance is measured. Since R_{wire2} is much higher compared to R_{sample}, very little current goes through R_{wire2} and therefore the voltage measured is the voltage across point A and B.

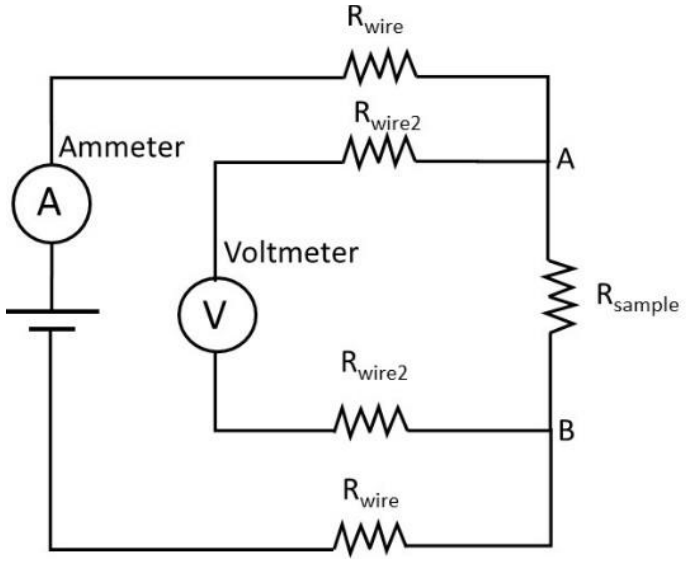

Figure 38: Schematic of 4-point resistance measurement

The measurement should be performed at a temperature below the critical temperature of 1.2 K of aluminum. In this case, the base temperature was 0.3 K. Figure 39 shows the I-V curve at base temperature 0.3 K and liquid He temperature, 4.2 K. These are unexpected results and the curve is linear at for both the junctions. However, there is a slight change of slope for the 2nd junction at around 0.3 mV but this cannot be attributed to the breaking of the cooper pairs since the leakage current is linearly increasing and not a constant value.

One feature of a good junction is the high ratio of maximal tunnelling current at the 2Δ edge to the leakage current below 2Δ. The ratio cannot be calculated in this case because it is

not observable. The possible reasons for these observations could be the quality of the junctions the possible reason for this is that the junction might be shorted because of pinholes in the junction or the resistances of the leads used for making the connection with the source meter.

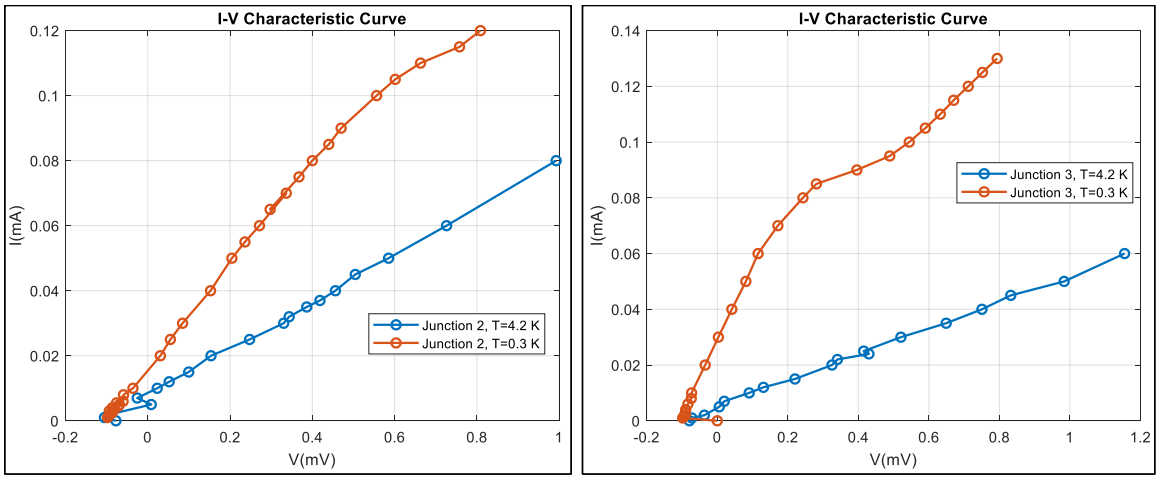

(a) (b)

Figure 39: I-V Curve at different temperatures

When we finally got Mr SQUID to work, we ran out of liquid Helium to could not achieve the base temperature of 0.3 K. Therefore, the measurements using Mr SQUID were done at 4.2 K. Figure 40 shows the I-V curve at 4.2 K using Mr SQUID. Comparing these results with the ones for source meter for the corresponding junctions, showed the resistance of a particular junction to be 10 times lower using Mr SQUID. Junction 1 and 2 graphs coincide indicating a possibility of pinhole through the insulating barrier because these junctions have different areas and therefore should have different resistances. Apart from that, the resistances measured using the two devices do not match. The junction were most likely destroyed or shorted due to improper storing and improper wire bonding of the tunnel junctions.

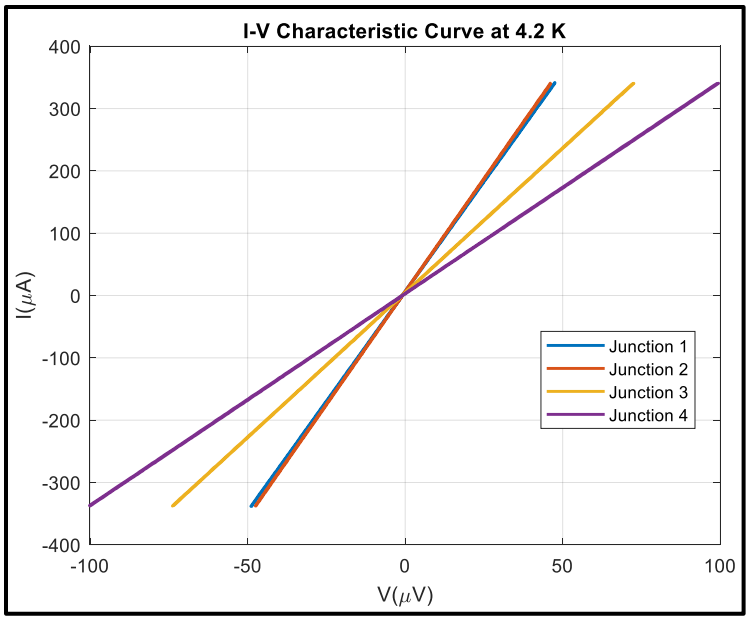

Figure 40: I-V curve using SQUID

CONCLUSIONS AND FUTURE WORK

The objective of this project was to revitalize an old E-beam system to deposit thin films. The E-beam system was modified to do multiple angle deposition and carry out in-situ oxidation in the load lock without breaking the vacuum of the main chamber. The modifications were made by adding a load lock and a sample transfer line to the system that allowed the easy motion of sample in and out of the main chamber. The magnetic transfer line was allowed both linear and rotary motion of the sample. The angle of deposition was easily controlled using the transfer line. The deposition was utilized to perform a double angle deposition to fabricate an aluminum superconducting tunnel junction. This technique proved to be significantly faster than previous ways of fabricating tunnel junction that involved breaking the vacuum of the main chamber. The key objectives of this project to perform multiple angle deposition was successfully achieved and even allowed the length of overlap in a tunnel junction to be controlled by varying the deposition angles. However, when the fabricated aluminum tunnel junctions were tested using I-V measurements, the quality of the junctions was not as good as expected. The quality of the junctions could be improved by improving the vacuum of the main chamber and following the correct procedure while testing the tunnel junctions.

Future work

The motivation for this project was to set up a system that can be used to fabricate a device that can be used in phonon spectrometry. The next objective would be to fabricate tunnel junction on both sides of a silicon substrate as shown in Figure 41. This will be a

challenging task as the two STJs need line up perpendicular to each other. This may require a new photomask that is symmetrical when flipped over.

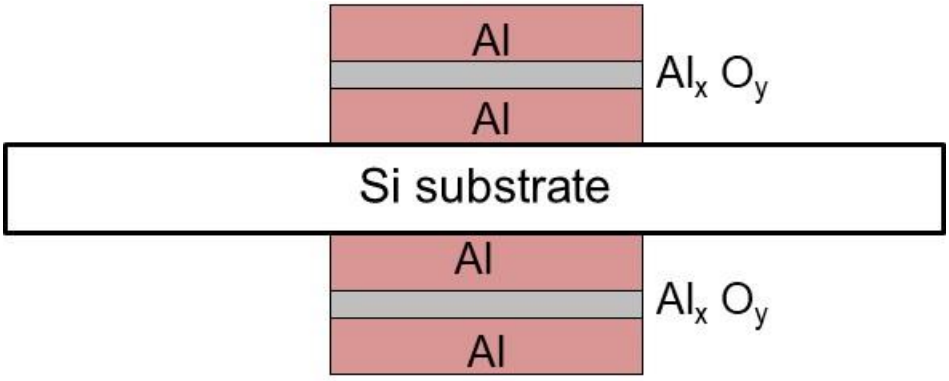

Figure 41: Aluminum STJ on both sides of the Si substrate

The ultimate goal is to fabricate a phonon spectrometer like the one shown in Figure 42. A phonon spectrometer is a useful device to determine the energy band gaps in nanocrystal superlattices. One of the STJ acts as the monochromatic phonon generator that sends activates phonons of a particular frequency and the other STJ will detect the phonons depending on the band gaps in the phononic crystal.

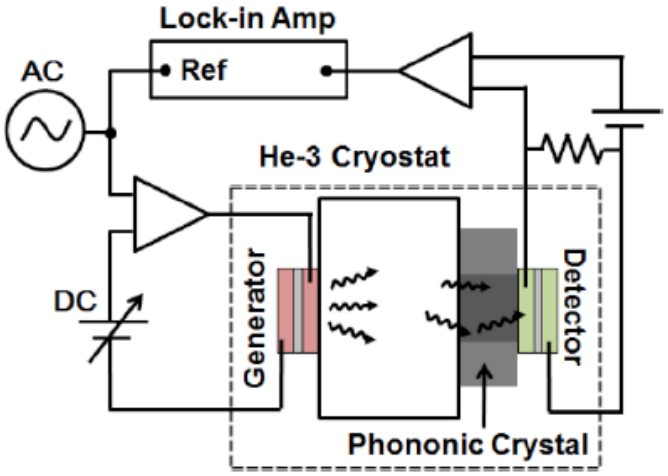

Figure 42: Phonon spectrometer

REFERENCES

1. Martin DDE, Verhoeve P. Superconducting tunnel junctions. *Obs Photons Sp*. 2013:479-496. doi:10.1007/978-1-4614-7804-1_27

2. Onnes HK. Communications - Leiden 120b. *Leiden Commun*. 1911;120b, 122b:261-272.

3. Meissner W, Ochsenfeld R. 787B_1.Tif. *Naturwissenschaften*. 1933;21(44):787-788. papers://215c83ae-6790-41ca-9965-80dd81ffbb77/Paper/p1344.

4. London F. On the problem of the molecular theory of superconductivity. *Phys Rev*. 1948;74(5):562-573. doi:10.1103/PhysRev.74.562

5. Bardeen J. Theory of the Meissner effect in superconductors [12]. *Phys Rev*. 1955. doi:10.1103/PhysRev.97.1724

6. Cooper LN. Bound electron pairs in a degenerate fermi gas [1]. *Phys Rev*. 1956. doi:10.1103/PhysRev.104.1189

7. Tinkham M. *Introduction to Superconductivity*. New York: Dover Publications; 1975.

8. VanDuzer T, Turner CW. *Principles of Superconductive Devices and Circuits*.; 1999. doi:10.1109/mcd.2000.846018

9. McMillan WL. Transition temperature of strong-coupled superconductors. *Phys Rev*. 1968. doi:10.1103/PhysRev.167.331

10. Chew AD, Cameron A, Goodwin D, et al. Considerations for Primary Vacuum Pumping in Mass Spectrometry Systems. *Spectroscopy*. 2005.

11. Davis RP, Abreu RA, Chew AD. Dry vacuum pumps: A method for the evaluation of the degree of dry. *J Vac Sci Technol A Vacuum, Surfaces, Film*. 2002. doi:10.1116/1.582424

12. Rochester Institute of Technology. Chapter 6 Vacuum Pumps. 2008;(April). https://people.rit.edu/vwlsps/LabTech/Pumps.pdf.

13. VACUUM P. Turbopumps. VACUUM, PFEIFFER. https://www.pfeiffer-vacuum.com/en/. Published 2018.

14. Audi M, de Simon M. Ion pumps. *Vacuum*. 1987. doi:10.1016/0042-207X(87)90048-0

15. Schuurman W. Investigation of a low pressure penning discharge. *Physica*. 1967. doi:10.1016/0031-8914(67)90086-9

16. Rottländer H, Voss G, Umrath W. Fundamentals of leak detection. 2016;(199).

17. Andrej Pregelj, Marjan Drab, IEVT, Teslova 30 L, Miran Mozetic, ITPO, Teslova 30 L. LEAK DETECTION METHODS AND DEFINING THE SI. The 4th International Conference of Slovenian Society for Nondestructive Testing .

18. IGAWA A. Helium Leak Detector. *Shinku*. 2011;34(11):807-812. doi:10.3131/jvsj.34.807

19. Oberg P, Lingensjo J. Crystal film thickness monitor. *Rev Sci Instrum*. 1959;30(11):1053. doi:10.1063/1.1716421

20. Walker CT. Low Temperature Solid State Physics. Some selected topics. H. M. Rosenberg. Oxford University Press, New York, 1963. xvi + 420 pp. Illus. $10.10. *Science (80-)*. 2006. doi:10.1126/science.145.3631.477-a

21. Fickett FR. Aluminum-1. A review of resistive mechanisms in aluminum. *Cryogenics (Guildf)*. 1971. doi:10.1016/0011-2275(71)90036-1

22. Charles K. *Introduction To Solid State Physics 8Th Edition.*; 2003. doi:10.1103/PhysRev.108.1175

23. Ashcroft NW, Mermin ND. *Solid State Physics*. Harcourt College Publishers

24. Krueger WH, Pollack SR. The initial oxidation of aluminum thin films at room temperature. *Surf Sci*. 1972;30(2):263-279. doi:10.1016/0039-6028(72)90002-7

25. De Vries JWC. Temperature and thickness dependence of the resistivity of thin polycrystalline aluminium, cobalt, nickel, palladium, silver and gold films. *Thin Solid Films*. 1988;167(1-2):25-32. doi:10.1016/0040-6090(88)90478-6

26. Hanaoka Y, Hinode K, Takeda K, Kodama D. Increase in Electrical Resistivity of Copper and Aluminum Fine Lines. *Mater Trans*. 2005;43(7):1621-1623. doi:10.2320/matertrans.43.1621

27. Meaden GT. *ELECTRICAL RESISTANCE OF METALS*. (Plenum Press NY, ed.). Plenum Press, New York,; 1965.

28. Lesker KJ. Linear & Rotary PowerProbe. 1845:8-9.

29. MicroChemicals. MicroChemicals ®-Fundamentals of Microstructuring - Lift-Off. www.microchemicals.com/downloads/application_notes.html.

30. Package D. AZ 3312 Photoresist.

31. Price LE. Recent german advances in the mechanism of oxidation and tarnishing of metals. *J Soc Chem Ind*. 1937. doi:10.1002/jctb.5000563503

32. Cabrera N, Mott NF. Theory of the oxidation of metals. *Reports Prog Phys*. 1949. doi:10.1088/0034-4885/12/1/308

33. Mott NF. The theory of the formation of protective oxide films on metals. - III. *Trans Faraday Soc*. 1947. doi:10.1039/TF9474300429

34. Troxtell C, Huckabee J. Electrostatic Discharge (ESD) Protective Semiconductor Packing Materials and Configurations. 2002;(April):1-16.

35. Pocock RN. Choosing the right bag. *Consult Specif Eng*. 2008;44(5 SUPPL.):9-10.

36. Populated I, Mckeon J, Control ESD, The B. ESD BAGS : TO SHIELD OR NOT TO SHIELD : 1999;(August).

37. Rowell JM. Tunneling Density of States-Experiment. In: Burstein E, Lundqvist S, eds. *Tunneling Phenomena in Solids: Lectures Presented at the 1967/NATO Advanced Study Institute at Risö, Denmark*. Boston, MA: Springer US; 1969:273-286. doi:10.1007/978-1-4684-1752-4_20

38. Brinkman WF, Dynes RC, Rowell JM. Tunneling conductance of asymmetrical barriers. *J Appl Phys*. 1970;41(5):1915-1921. doi:10.1063/1.1659141

39. Simmons JG. Generalized Formula for the Electric Tunnel Effect between Similar Electrodes Separated by a Thin Insulating Film. *J Appl Phys*. 1963;34(6):1793-1803. doi:10.1063/1.1702682

40. Zhang ZS, Rabson DA. Electrical and thermal modeling of the non-Ohmic differential conductance in a tunnel junction containing a pinhole. *J Appl Phys*. 2004;95(2):557-560. doi:10.1063/1.1633341

41. Åkerman JJ, Guedes I, Leighton C, Grimsditch M, Schuller IK. Upper bound for the magnetic proximity effect extracted from Brillouin light scattering. *Phys Rev B - Condens Matter Mater Phys*. 2002;65(10):1044321-1044324. doi:10.1103/PhysRevB.65.104432

42. Jönsson-Åkerman BJ, Escudero R, Leighton C, Kim S, Schuller IK, Rabson DA. Reliability of normal-state current - Voltage characteristics as an indicator of tunnel-junction barrier quality. *Appl Phys Lett*. 2000. doi:10.1063/1.1310633

43. Miller FLE, Mallison WH, Kleinsasser AW, Laboratories TB, Hill M. Niobium Mayer Josephson current densities tunnel junctions with ultrahigh critical. 2001;63(10):1423-1425.

APPENDIX A

STANDARD OPERATING PROCEDURE FOR E-BEAM SYSTEM

A1 Loading and transferring the sample:

1. To load the sample, open the 6-inch flange with view window on the load lock.
2. Unscrew the sample holder shown in Figure 44 from the transfer line. Use the Allen key to loosen the clamp on the sample holder. Tighten the clamp with the sample.
3. Put the sample holder back with the samples. Close the view window (use new copper gasket to avoid any leak).
4. Open the gate valve shown in Figure 43 and move the sample in the center of the main chamber. The linear lock can be unscrewed and fixed at any appropriate place. It is already in the correct place.
5. Unlock the rotational motion. Adjust the angle of the sample using the dial on the magnetic transporter.

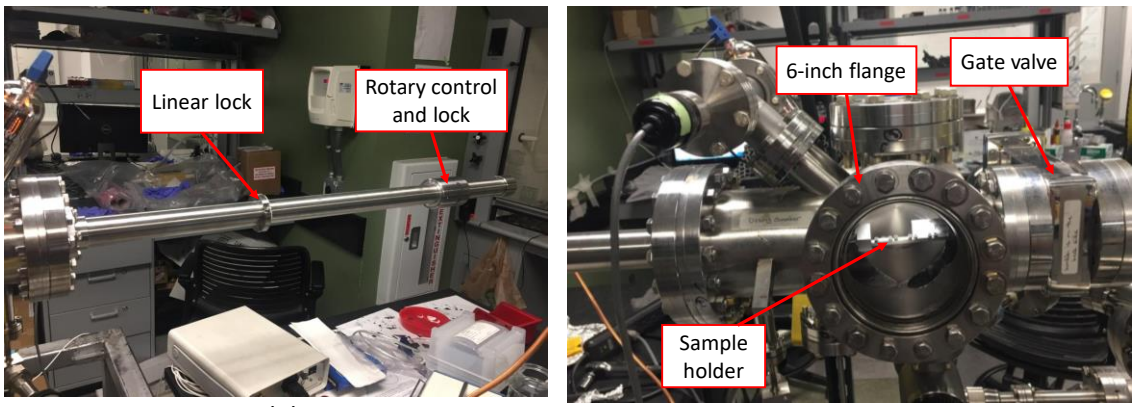

Figure 43: Load lock and magnetic transfer line

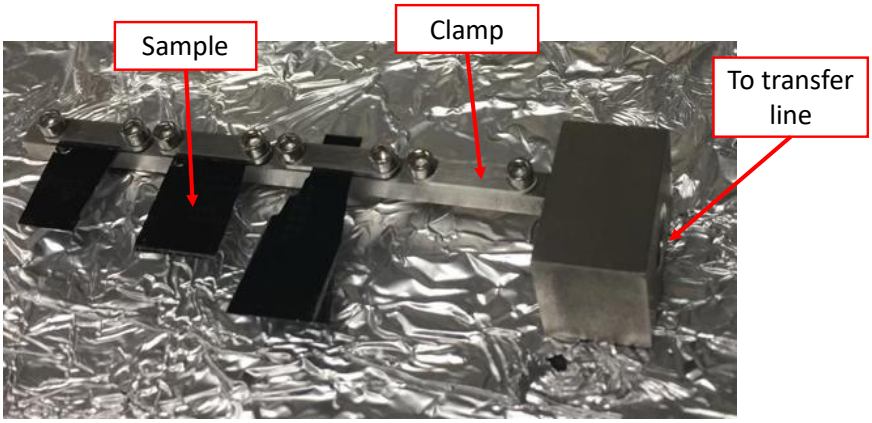

Figure 44: Sample holder

A2. Loading the material:

1. Open the 6-inch flange shown in Figure 45 on the main chamber.
2. To minimize opening the main chamber, load the all 3 crucibles with aluminum.

   Note: For the front E-gun, only one crucible holder is working properly.
3. Create a bridge with aluminum foil between crucible holder and edge of the window to avoid the crucible falling inside the chamber.
4. Use the tweezers to pick and drop the crucible in their respective locations.
5. Clean the crucible thoroughly to remove coatings built-up from previous depositions. Load the crucible along with source material with the help of tweezers in one the crucible holders on the e-Gun(front) body.
6. Close the flange. Always use a new copper gasket.

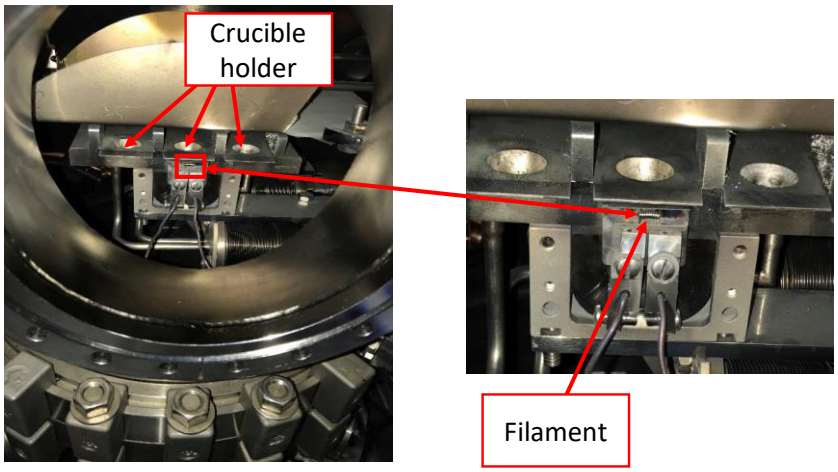

Figure 45: Crucible holder and filament

A3. Pumping:

A3.1 Mechanical/ roughing pump

1. Before pumping, make sure all the flanges on the main chamber and load lock are properly tight. Connect the mechanical pump to the bellows. Make sure the gate valve is open.
2. Pump using this pump for half an hour. You will reach a pressure of about 200 mTorr that can be read using TC gauge. Close the valve that connect the pump and load lock.
3. The gas ballast is opened when there is a water vapour condensation in the pump. Gas ballast must be opened for 2-3 seconds and closed instantly.

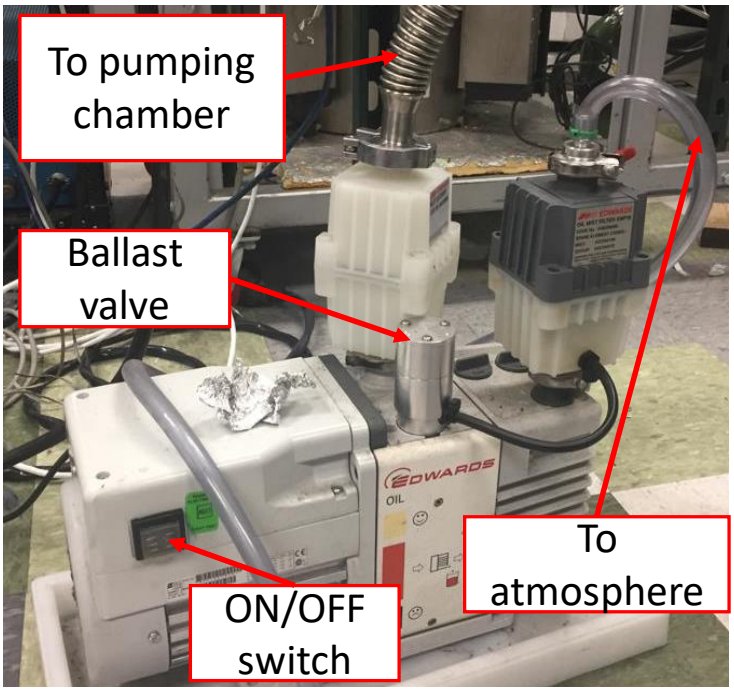

Figure 46: Mechanical/ roughing pump

A3.2 Turbo pump

1. Disconnect the bellows from mechanical pump and connect it to the turbo pump.
2. Begin pumping of the system by first turning ON the turbo pump. Wait for the preloaded setup to complete (can be seen on display panel). Then select parameter number 340 (Pressure) using the arrow keys and then press start.
3. Let the turbo pump run for about 5-7 minutes. It should reach a pressure level of 7 x 10^{-5} mbar. Once this pressure is reached, open the gate valve with the torque wrench connected to upper chamber gradually in successive steps i.e. not at once.
4. *NOTE: The gate valve needs to be opened gradually because of two reasons:*

   i) The main reason being the large volume of the chamber. If you open the gate valve all at once, the sudden inrush of high pressure (i.e. high gas throughput)

from the chamber into the turbo pump might lead to overheating of the pump and ultimately lead to its failure. Since there are rotating parts in the pump at high speed, the failure may cause the rupture of the pump body and the blades coming off from the rotor.

ii) The pump may face the issue of condensable vapors desorbing from the large volume of the chamber surface.

Even after opening the gate valve gradually if you face the problem of high base pressure, close the gate valve completely. Disconnect the turbopump from the system and cap the open end of the turbo pump. Open the gas ballast valve by pushing the sleeve as shown in the Fig 10. On the panel, go to Parameter number 23(Motor pump) and turn it OFF. To change from ON state to OFF state, press both the arrow keys simultaneously, then press the right arrow key. This should turn OFF the Motor pump. Again, press both the arrow keys simultaneously to confirm the change. Go to Parameter no 340 and press start. Let the pump run for an hour with the ballast valve open. After running for an hour, the required base pressure should be reached. Now, turn OFF the pump and close the gas ballast valve. Wait for the rotor to stop completely (Usually takes 5-7 minutes) and then vent the pump to atmosphere using the valve at the back of the pump. Reconnect the pump to the system, turn ON the Motor pump and repeat.

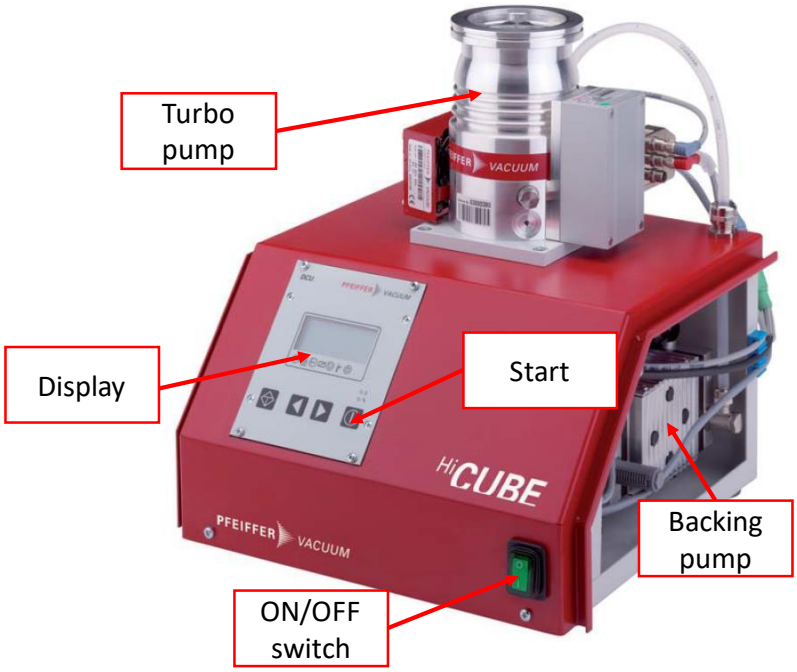

Figure 47: Turbo pump

A3.3 Ion pump

1. Put the Ion pump power supply in start mode. Turn it on by pressing the ON button. The high voltage neon bulb on the front panel will light indicating that the voltage is being applied. The neon bulb above the START-PROTECTION switch will also light indicating that the switch is in Start Position.

2. Do not turn OFF the turbo pump immediately. The pressure starts to drop quickly. Change the meter range according to the reading on the scale. Once the current is in the 2mA range, switch to Protection mode. *WARNING: The operator of the system should be present near the system to use the Ion pump power supply in the Start mode.*

3. *NOTE:*

    a. *The START-PROTECTION switch needs to be in the PROTECTION mode to protect the pump and the control unit in the event of an unattended pressure rise.*

    b. *The Protection mode consists of a circuit breaker that turns off the control unit if the current is above 130mA. Previously we faced the issue of circuit breaker turning off the control unit even when the current was below 130 mA. This was caused due to a contaminated connection in the circuit breaker. In such a case, contact Richard Hanley for helping with cleaning of the contaminated connection.*

    c. *Another possibility for the circuit breaker to turn off the control unit is damage of one of the insulating plates on the pump. This can be checked by removing the high voltage connection of the pump and checking the resistance of the high voltage feedthrough with the ground using a 20-ohm (or greater) resistance meter. There should not be any resistance when checking with ground; if the meter shows a resistance it means that there is overlap of the insulator plates inside the pump leading to short circuit.*

4. After switching the Ion pump to protection mode, the Turbo pump can be turned OFF. Make sure the gate valve is close before the turning OFF turbo pump. *WARNING: After turning OFF the Turbo pump wait for the rotor to stop completely and only then vent it to the atmosphere.*

5. Monitor the pressure in the chamber by turning ON the Ion gauge power supply shown in Figure 49. The Ion gauge can be turned ON by using the Toggle switch indicated as ON-OFF. The red neon light turns on indicating that the gauge is on. Then turn ON the filament by using the Toggle switch indicated as ON-FIL. The green neon light turns on indicating that the filament is on. If the filament toggle switch flips back, it means that the pressure in the system is still too high to be read by Ion gauge. Typically, the Ion gauge reads pressures less than 1 x 10^{-3} Torr. The system should reach a base pressure of 1 x 10^{-7} Torr.

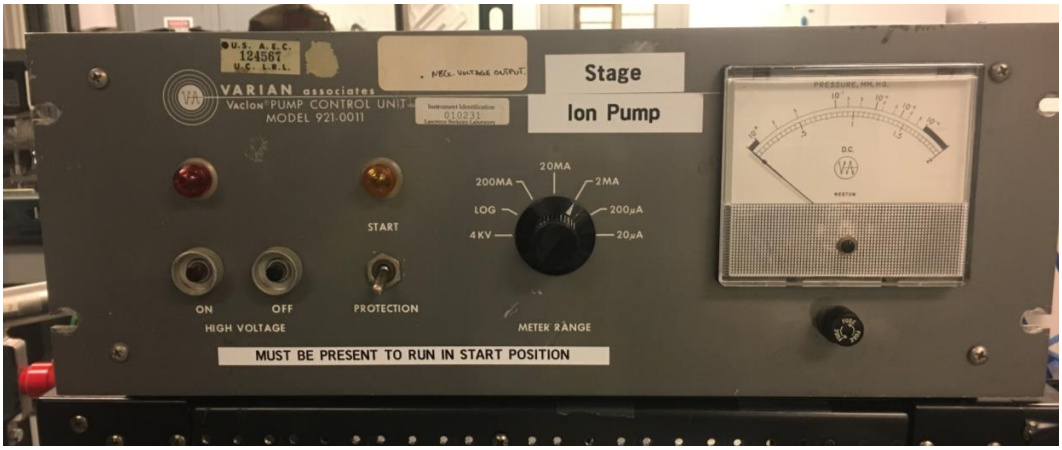

Figure 48: Ion pump power supply/ control unit

Figure 49: Ion gauge power supply/ control unit

A4. Cooling water

1. The cooling water is needed to cool the crucible as well as the thickness monitor. Depending on which e-gun is in use, make the required connection. Use the screw driver to loosen or tighten the clamps.

2. To start the water flow, turn both the valves in the vertical direction. If there is a leak, Turn OFF water flow and use Teflon tape to make water tight connections.

3. Let water run for 5-7 minutes before starting the deposition.

4. In case of any major problem or help, contact Fred Pena.

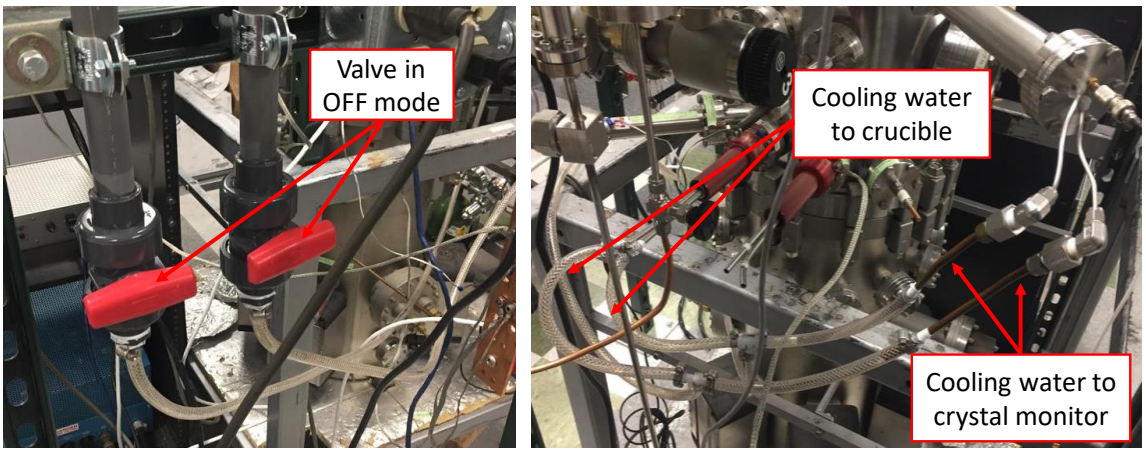

Figure 50: Cooling water arrangement

A5. Film deposition

1. Ensure that the sample is at the correct angle at which you wish to perform the deposition.

2. Turn on the cooling water. Open both inlet and exit valve ensure the continuous supply of fresh water from the building. Let he water run for 5-7 minutes.

3. Before proceeding further, ground all the parts involved in the experiment i.e. e-gun power supply, chamber, e-gun etc.

4. To ground, use the grounding wire to connect the above-mentioned parts to grounding bar on the frame.

5. Cover the sample with the shutter. This is to ensure a constant deposition rate.
6. Insert the E-guns into the inserts shown in Figure 52. Turn ON main switch on the E-gun power supply. Turn it OFF if there is any spark or unusual activity.

7. Turn ON high voltage and wait for 2 minutes.
8. Slowly increase the increase the emission current using the emission current control. Do not go beyond 10 mA. Wait for the emission current to stabilize at this value. In this manner, increase the current to a desired value. This is done to avoid any unwanted current spikes. It's been observed that slowly increasing the current prevents any spikes.

9. Once its stable, open the shutter and allow the deposition to happen for a specific time or thickness. During deposition, emission current drifts. Adjust the value using a emission current control to maintain a constant current value.

10. Monitor the deposition rate and thickness using the thickness monitor shown in Figure 53. The red shutter button resets the deposition thickness to zero. Press this button when the shutter is open.

11. To observe the filament or sample during this time, use safety goggles.

12. After the deposition, cover the sample with the shutter. Gradually decrease the emission current to 0. Turn OFF the high voltage and main switch.

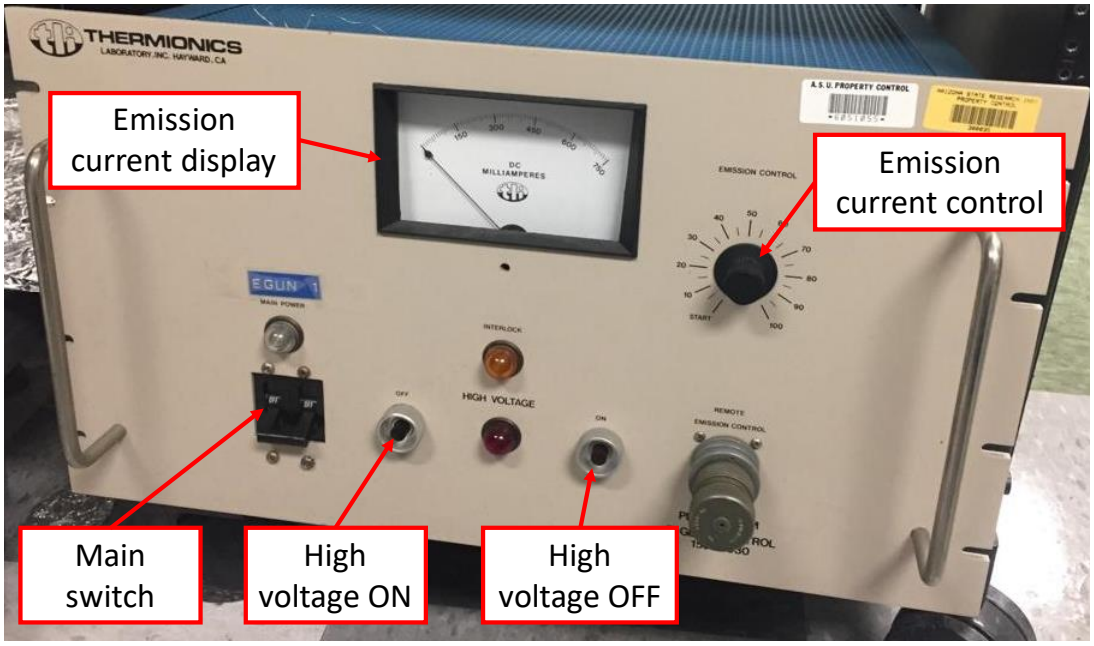

Figure 51: E-gun power supply/ control unit

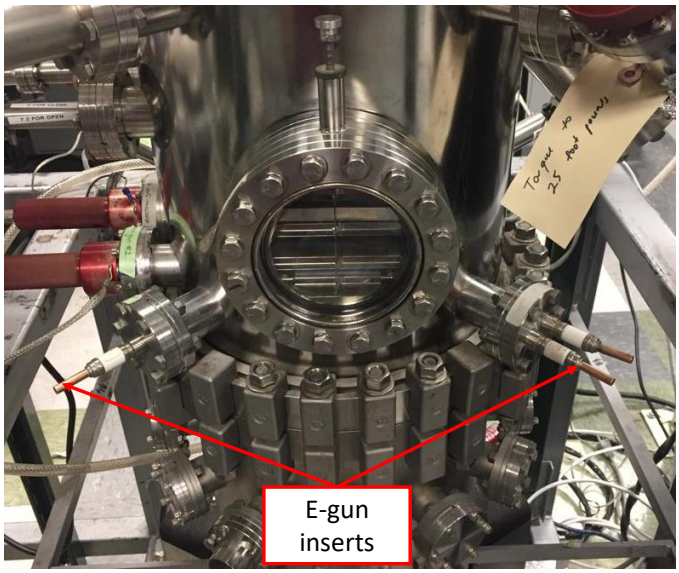

Figure 52: E-gun inserts

Figure 53: Thickness monitor control/display

A6. Oxidation

1. Oxidation need to be carried out in the load-lock. Make sure all the openings are closed and load lock pressure is same as the that of the chamber.

2. Transfer the sample using the magnetic transporter into the valve and close the gate valve.

3. Use the regulator to start the gas flow from the gas cylinder. Slowly open the control valve shown in Figure 55 to control the pressure. close the valve once the desired pressure is reached.

4. Monitor the pressure in the load lock using the TC gauge.

5. Carry out oxidation process at desired pressure and for a certain time.

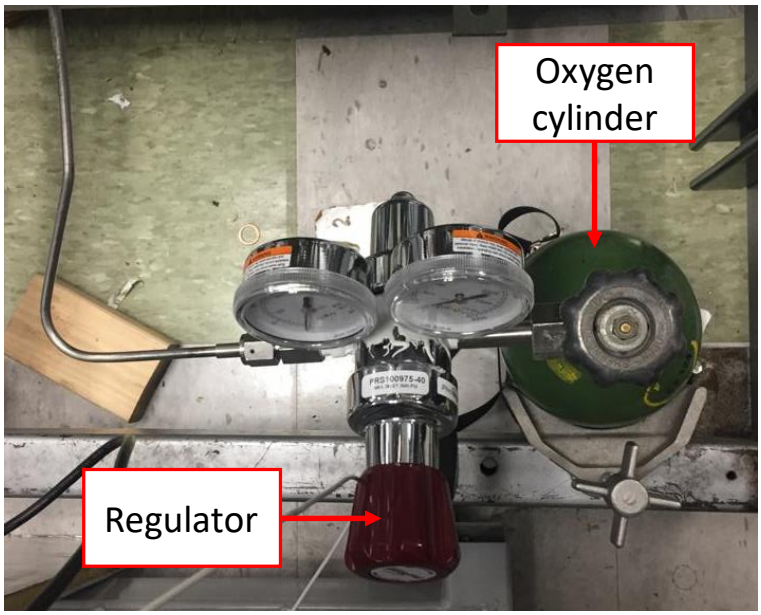

Figure 54: Oxygen cylinder

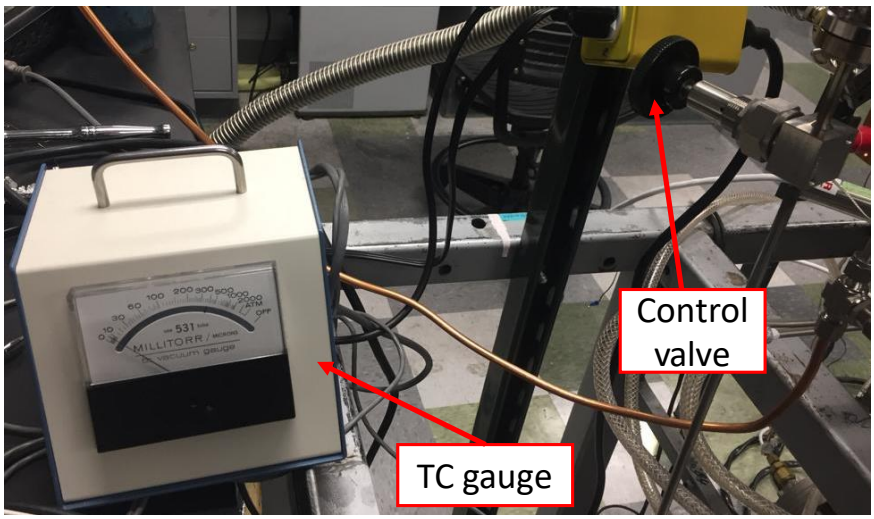

Figure 55: TC gauge and control valve